



HAL
open science

Thermosolutal convection and macrosegregation during directional solidification of TiAl alloys in centrifugal casting

Martín Cisternas Fernández, Miha Založnik, Hervé Combeau, Ulrike Hecht

► To cite this version:

Martín Cisternas Fernández, Miha Založnik, Hervé Combeau, Ulrike Hecht. Thermosolutal convection and macrosegregation during directional solidification of TiAl alloys in centrifugal casting. *International Journal of Heat and Mass Transfer*, 2020, 154, pp.119698. 10.1016/j.ijheatmasstransfer.2020.119698 . hal-02546766

HAL Id: hal-02546766

<https://hal.science/hal-02546766v1>

Submitted on 18 Apr 2020

HAL is a multi-disciplinary open access archive for the deposit and dissemination of scientific research documents, whether they are published or not. The documents may come from teaching and research institutions in France or abroad, or from public or private research centers.

L'archive ouverte pluridisciplinaire **HAL**, est destinée au dépôt et à la diffusion de documents scientifiques de niveau recherche, publiés ou non, émanant des établissements d'enseignement et de recherche français ou étrangers, des laboratoires publics ou privés.

Thermosolutal convection and macrosegregation during directional solidification of TiAl alloys in centrifugal casting

Martín Cisternas Fernández^{a,*}, Miha Založnik^a, Hervé Combeau^a, Ulrike Hecht^b

^a*Université de Lorraine, CNRS, IJL, F-54000 Nancy, France*

^b*Access e.V., Intzestr. 5, D-52072 Aachen, Germany*

Abstract

Experiments of directional solidification of TiAl cylindrical samples were conducted within the frame of the ESA GRADECET project. The experiments were performed in the ESA “Large Diameter Centrifuge” using a furnace with a well defined thermal protocol. The furnace was mounted in the centrifuge and free to tilt in such a way that the total apparent gravity (sum of terrestrial gravity and centrifugal acceleration) was aligned to the cylinder centerline. Several centrifugation levels were investigated besides to one reference case out of the centrifuge. In this work, we present 3D numerical simulations of these experiments paying special attention in the liquid thermosolutal buoyancy convection and aluminum macrosegregation. The numerical model accounts for the non-inertial accelerations that appear in the rotating reference frame (centrifugal and Coriolis), motionless solid, thermosolutal Boussinesq approximation and an infinitely fast microscopic diffusion model between the phases to depict the solid growth. The results showed that the Coriolis acceleration entirely modifies the liquid flow regime during solidification leading to a 3D aluminum segregation pattern with respect to the case solidified under normal terrestrial gravity conditions. Additionally the magnitude of aluminum segregation increases with the level of centrifu-

*Corresponding author

Email addresses: martin.cisternas-fernandez@univ-lorraine.fr (Martín Cisternas Fernández), miha.zaloznik@univ-lorraine.fr (Miha Založnik), herve.combeau@univ-lorraine.fr (Hervé Combeau), u.hecht@access-technology.de (Ulrike Hecht)

Preprint submitted to International Journal of Heat and Mass Transfer

gation.

Keywords: centrifugal casting, macrosegregation, thermosolutal convection, Titanium-aluminide alloys

1. Introduction

Titanium-aluminide alloys have been studied for more than 20 years due to their low density and their high strength in high temperature environments. These properties make them a good candidate for aerospace and automobile applications [1]. However, their high reactivity in liquid state makes them difficult to cast since great superheated liquid enables undesired chemical reactions. In case of γ (TiAl) small traces of H, C, N or O increase dramatically their embrittlement [2]. Centrifugal casting is an option to enhance mold filling speed due to the combined effect of terrestrial gravity and centrifugal acceleration that push the liquid inside the mold. This technique permits to cast with a low superheated liquid and to avoid porosity or undesired chemical reactions.

Two specific phases of TiAl have attracted engineering attention: α_2 (Ti₃Al) and γ (TiAl). A mixture of these two phases ($\alpha_2 + \gamma$) exists when the aluminum concentration is between 40at% and 48at%. It has been shown that the proportion of these two phases in the final cast part is highly sensitive to the aluminum concentration [1]. Moreover, aluminum concentration can also affect the grain size and the columnar-to-equiaxed transition [3]. Therefore, the control of aluminum segregation is an important key to the control of microstructure formation during solidification.

Macrosegregation is the heterogeneity in solute composition produced during solidification at the product scale. It is induced by the relative movement between the solid and the liquid phases, which have different compositions because they do not admit the same amount of solute at a given thermodynamic state. One of its causes is the liquid thermosolutal buoyancy driven convection. In case of centrifugal casting, the buoyancy driven flow is directly modified by the combined effect of the non-inertial accelerations – centrifugal and Coriolis – which appear in the rotating reference system. Their effect on the solidification of crystals have been studied extensively in the nineties. Indeed, Rodot et al. [4] performed experiments of crystal growth in a Bridgman furnace mounted in a centrifuge. In our knowledge, they were the first to relate segregation of alloying elements to

different fluid flow regimes produced under centrifugation. Müller et al. [5] also performed experiments of crystal growth in centrifuges using different configurations. They found that the liquid thermal buoyancy driven convection can be present in two different regimes which depend on the Rayleigh number and the aspect ratio of the growing crystal. Later, Ramachandran et al. [6], by means of numerical simulations and scaling analysis, completed the explanation of these two different flow regimes concluding that the Coriolis force plays a fundamental role determining the liquid flow features. More recently, Yang et al. [7] investigated the centrifugal investment casting of low pressure turbine blades for high Nb -TiAl alloys paying attention in the analysis of porosity and cracks formation. However, they did not characterize the resulting liquid thermosolutal convection nor take into account the Coriolis acceleration. Although Coriolis acceleration is known to produce different kind of liquid flow regimes and to modify the complete fluid flow structure, its impact on thermosolutal buoyancy driven flows during solidification has not been studied yet.

The European Space Agency (ESA) launched the GRADECET (“GRAvity DEpendance of Columnar to Equiaxed Transition”) project, whose main objective is to investigate the influence of gravity on the Columnar to Equiaxed Transition – *CET* – and on microstructure formation in peritectic TiAl alloys. Within the framework of this project, several experiments of directional solidification in hypergravity were carried out in the ESA “Large Diameter Centrifuge” (LDC). These experiments gave relevant information on the solidification microstructure formed under different gravity levels [8]. To fully understand the experimental observations, characterizations of the liquid thermosolutal convection during solidification is needed. This work aims to support the understanding of the liquid convection by means of numerical simulations.

In this work, we present numerical simulations of the GRADECET experiments performed with a solidification model for columnar growth that takes into account the centrifugal and Coriolis accelerations that appear in the non-inertial rotating reference system. The simulations were carried out by using “macroS3D” [9, 10], which is a numerical solver based in the finite-volume framework OpenFOAM. We show that the Coriolis force has a large impact on the aluminum segregation because it breaks the fluid flow symmetry leading to an entirely three-dimensional aluminum segregation pattern.

2. Model

The solidification model is identical to the one used by Cisternas-Fernández et al. [11]. The model takes into account heat transfer, solute transport, buoyancy driven liquid flow and solidification of a binary alloy. We use the volume-averaging method [12, 13, 14] to formulate conservation equations for mass, momentum, energy and solute. The equations are formulated in terms of averaged quantities, such as averaged intrinsic liquid velocity, $\langle \vec{v}_l \rangle^l$, averaged enthalpy, $\langle h \rangle$, and averaged solute concentration, $\langle C \rangle$, respectively. The equations are formulated for a non-inertial reference frame, therefore the momentum equation accounts for the centrifugal and Coriolis accelerations [15, 10]. The Kozeny-Carman relation is used to calculate the hydrodynamic permeability of the mushy zone, K , and the Boussinesq approximation is employed to take into account the thermosolutal buoyancy driven flow. The solid and liquid densities are considered to be equal, therefore, the solidification shrinkage effect is not included in the model. The solid phase is considered to be fixed in the domain, *i.e.* $\langle \vec{v}_s \rangle^s = 0$, since the model only represents columnar growth.

The energy conservation equation is formulated in terms of the averaged enthalpy $\langle h \rangle = c_p T + g_l L_f$, where c_p is the specific heat, T the temperature, L_f the latent heat, and g_l the liquid fraction. The specific heat is considered constant and equal between the phases, $c_{pl} = c_{ps} = c_p$. The local temperature is assumed to be equal in the solid and liquid phases, $T = T_s = T_l$.

Finally, the solid-liquid phase change is represented by an equilibrium model that assumes infinitely fast diffusion at the microscopic scale (lever rule). This equilibrium model is taken into account in order to simplify the overall model and still be able to depict the liquid thermosolutal convection and the solute segregation pattern. The diffusion at the macroscopic scale is neglected. The full description of the volume-averaged solidification model is presented below.

- *Mass conservation:* Only the liquid movement is considered.

$$\nabla \cdot \left(g_l \langle \vec{v}_l \rangle^l \right) = 0 \quad (1)$$

- *Liquid momentum conservation:*

$$\begin{aligned} \frac{\partial}{\partial t} \left(g_l \langle \vec{v}_l \rangle^l \right) + \nabla \cdot \left(g_l \langle \vec{v}_l \rangle^l \langle \vec{v}_l \rangle^l \right) + 2g_l \left(\vec{\omega} \times \langle \vec{v}_l \rangle^l \right) = \\ - \frac{g_l}{\rho} \nabla p + \nabla \cdot \left(g_l \nu_l \nabla \langle \vec{v}_l \rangle^l \right) - \frac{\nu_l g_l^2}{K} \langle \vec{v}_l \rangle^l + \frac{g_l \rho_l^b}{\rho} [\vec{g} - \vec{\omega} \times (\vec{\omega} \times \vec{x}_c)] \end{aligned} \quad (2)$$

Where $\rho_l^b = \rho \left(1 - \beta_T (T - T_{ref}) - \beta_C (\langle C_l \rangle^l - C_{ref}) \right)$ and $K = \frac{\lambda_2^2 g_l^3}{180(1-g_l)^2}$

- *Energy conservation:*

$$\frac{\partial \langle h \rangle}{\partial t} + \nabla \cdot \left(g_l \langle \vec{v}_l \rangle^l \langle h_l \rangle^l \right) - \frac{1}{\rho} \nabla \cdot (k \nabla T) = 0 \quad (3)$$

Where $\langle h_l \rangle^l = c_p T + L_f$ and $\langle h \rangle = c_p T + g_l L_f$.

- *Solute conservation:* Macroscopic solute diffusion is neglected.

$$\frac{\partial \langle C \rangle}{\partial t} + \nabla \cdot \left(g_l \langle \vec{v}_l \rangle^l \langle C_l \rangle^l \right) = 0 \quad (4)$$

- *Liquid fraction:* An invariant point at the temperature $T_{per} = T_f + m_l C_{inv}$ is considered

$$g_l = \begin{cases} 1.0 & \text{if } \langle h \rangle > h_{liq} \\ 0.0 & \text{if } \langle h \rangle < h_{sol} \\ \frac{\langle h \rangle - c_p T_{per}}{L_f} & \text{if } c_p T_{per} < \langle h \rangle < h_{per} \\ \frac{-B + \sqrt{(B^2 - 4A \cdot V)}}{2A} & \text{otherwise} \end{cases} \quad (5)$$

Where,

$$h_{liq} = c_p \max(T_f + m_l \langle C \rangle, T_{per}) + L_f$$

$$h_{sol} = c_p \max\left(T_f + \frac{m_l}{k_p} \langle C \rangle, T_{per}\right)$$

$$h_{per} = c_p T_{per} + \frac{L_f (\langle C \rangle - k_p C_{inv})}{(1 - k_p) C_{inv}}$$

$$A = \frac{L_f (k_p - 1)}{c_p m_l}$$

$$B = \frac{\langle h \rangle (1 - k_p) - k_p L_f}{c_p m_l} + \frac{T_f (k_p - 1)}{m_l}$$

$$V = \frac{k_p \langle h \rangle}{c_p m_l} - \frac{k_p T_f}{m_l} - \langle C \rangle$$

- *Supplementary relations:*

- Averaged solute concentration:

$$\langle C \rangle = g_l \langle C_l \rangle^l + (1 - g_l) \langle C_s \rangle^s \quad (6)$$

- Solid - liquid equilibrium relations:

$$T = T_f + m_l \langle C_l \rangle^l \quad (7)$$

$$\langle C_s \rangle^s = k_p \langle C_l \rangle^l \quad (8)$$

3. Case study

The GRADECET hypergravity experiments consisted of the directional solidification of cylindrical TiAl samples (8 mm diameter and 165 mm long) in the ESA Large Diameter Centrifuge (“LDC”). The custom designed directional solidification furnace was placed in a gondola fixed at the end of the arm of the centrifuge, at a distance of 4 m from the rotation axis. The gondola was free to tilt, such that the total apparent gravity, \vec{g}_{tot} , – the sum of the terrestrial gravity and centrifugal acceleration – was always aligned with the sample centerline. Four centrifugation speeds were used, corresponding to gravity levels of 5g, 10g, 15g and 20g where g is the terrestrial gravity acceleration. Additionally, a case in which $\vec{g}_{tot} = 1g$ was performed without centrifugation, under terrestrial gravity aligned with the sample centerline.

The thermal protocol consisted of three stages: remelting of the initially solid sample, holding and solidification. It was driven by three temperature controlled heaters placed around the crucible, as shown in Fig. 1. During the solidification stage the thermal protocol was adjusted in order to induce

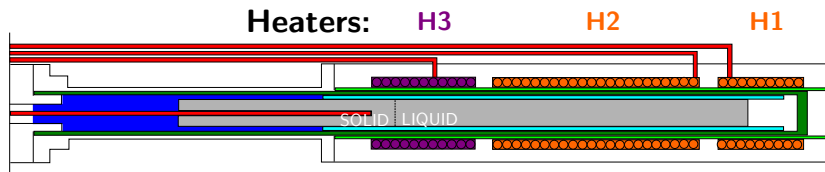


Figure 1: Schematic of the sample, heaters and thermocouples (adapted from ref. [8]). The thermocouples are represented by the red wires and the heaters by purple (“H3”) and orange (“H1” and “H2”) circles. At $t = 0$, the heaters temperatures are $T_{H1} = 1623\text{ }^{\circ}\text{C}$, $T_{H2} = 1623\text{ }^{\circ}\text{C}$ and $T_{H3} = 1543\text{ }^{\circ}\text{C}$.

a temperature field that would promote a columnar-to-equiaxed transition. The remelting stage starts with a fully solid sample and the heaters increase their temperature until the sample is partially melted. Following, in the holding stage, all the heaters maintain their temperature for five minutes in order to stabilize the thermal profile within the sample. The solidification and last stage is divided in two sub-stages. In the first solidification sub-stage, the heater “H3” decreases its temperature at a cooling rate of 0.3 K s^{-1} for 120 s, while heaters “H1” and “H2” maintain their temperature. In the second solidification sub-step, the heater “H3” decreases its cooling rate to 0.1 K s^{-1} while “H1” and “H2” increase it to 0.4 K s^{-1} . This second-substage lasts 367 s implying that the total duration of the solidification stage is 487 s. At the end of the solidification stage, the sample is quenched, solidifying any remaining liquid. Time is defined as $t = 0$ at the beginning of the solidification stage. The temperature was sampled throughout each experiment by three thermocouples located in each heater and one located in the part of the sample that was not melted (Fig. 1). Figure 2 shows the temperature measured by the thermocouples over time, along with the corresponding protocol stages. In Figure 3 a schematic of the furnace configuration mounted in the centrifuge gondola is presented. More details on the experimental configuration are reported in reference [8].

The alloy composition was Ti-32.96 wt.%Al-2.49 wt.%Cr-4.76 wt.%Nb (Ti-47.46 at.%Al-1.86 at.%Cr-1.99 at.%Nb in atomic percent). This alloy undergoes a peritectic transformation in its solidification path near $1480\text{ }^{\circ}\text{C}$. In order to account for this transformation, a simulation of the solidification path was performed using Thermo-Calc Software considering full equilibrium between the phases. The multicomponent alloy was approximated by a pseudo-binary (Ti-Al) approximation that fits the full alloy in terms of solidification path, solute partitioning and evolution of the liquid density in

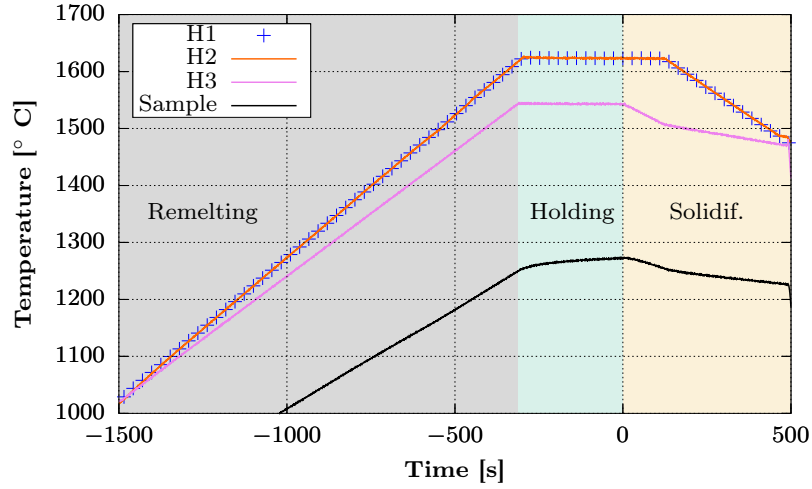


Figure 2: Temperature measured by the thermocouples in the three stages of the furnace protocol. The time $t = 0$ at the beginning of the solidification stage.

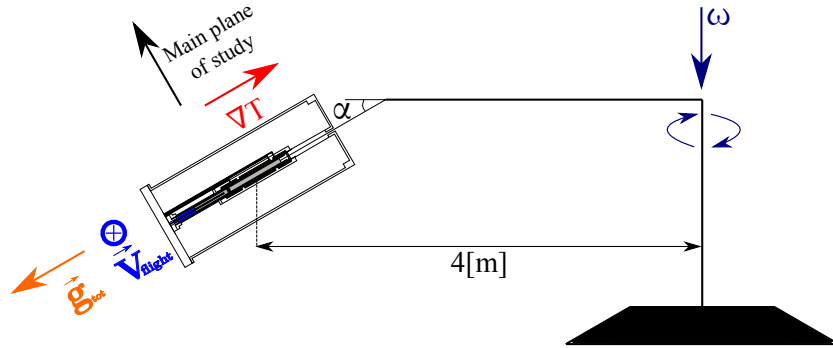
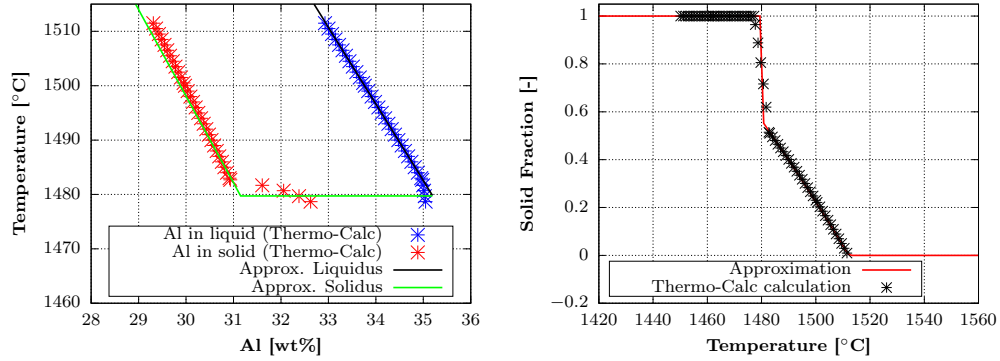


Figure 3: Schematic of the furnace and the TiAl sample in the centrifuge (adapted from ref. [8]). The sample is represented in grey and the heaters in orange and yellow. The furnace tilting angle is denoted by α , the furnace flight velocity by \vec{V}_{flight} and the total apparent gravity by \vec{g}_{tot} . The main plane of study is that formed by the total apparent gravity and flight velocity vectors. The normal vector to the main plane of study is shown in black.



(a) Averaged equilibrium concentration of aluminum in solid and liquid phases vs temperature.

(b) Solidification path

Figure 4: Results of the solidification path simulation using Thermo-Calc Software along with the approximations used in the this work (as reported in ref. [11]).

the mushy zone. Figure 4a presents the averaged aluminum concentration in solid and liquid phases obtained with Thermo-Calc and the approximation for the *liquidus* and *solidus* lines used in this work. Figure 4b presents the corresponding solidification path that assumes thermodynamic equilibrium between all phases along with the approximation of the solidification path used in this work. The simplified solidification path considers an invariant point – pseudo-peritectic – at $T_{per} = 1479.7^\circ\text{C}$. This simplification on the solidification path is valid under hypo-peritectic solidification. Yet, it can also be used as an approximation under hyper-peritectic solidification, in the neighborhood of the peritectic point, if a low peritectic phase formation is assumed. The nominal alloy composition used in this work is slightly hypo-peritectic and it is assumed that the formation of peritectic phase does not have a large impact on the solute segregation.

3.1. Numerical setup

Numerical simulations of the GRADECET experiments were conducted in order to understand the combined effect of the centrifugal and Coriolis accelerations on the liquid thermosolutal convection and on the aluminum macrosegregation. The domain of study was a cylinder 8 mm in diameter and 118 mm long since in the experiments the samples were not fully remelted. The domain was discretized with a structured hexahedral mesh, using the

standard OpenFOAM tool *blockMesh*. More details about the mesh structure are presented in the Appendix A. Only the solidification stage of the thermal protocol is simulated. The furnace is not included in the model.

Due to the complex design of the furnace, the heater temperatures can not be directly used as boundary conditions on the sample furnace. Numerical heat transfer simulations of the full furnace using a dedicated furnace model were performed and calibrated with temperature measurements to obtain realistic boundary conditions. From these simulations, the evolution of the temperature profile along the sample over time was extracted. The temperature information was imposed as a Dirichlet boundary condition on the surface of the TiAl sample in the solidification simulations. Figure 5 shows the temperature boundary conditions on the cylinder surface at different times. The initial temperature in the cylinder was assumed to be independent of the radius and to follow the temperature profile at $t = 0$. The initial solid fraction was determined from the temperature using the solidification path (see Fig. 4b). In addition, throughout the domain, at $t = 0$, the liquid intrinsic velocity was assumed to be null, and the aluminum concentration to be equal to the nominal concentration ($\langle C \rangle = 32.96 \text{ wt.}\%$). The characteristic length for the mushy zone permeability is assumed to be the secondary dendrite arm spacing, λ_2 , which was measured by means of post-mortem grain morphology characterizations of samples of the GRADECET experiments [8]. Table 1 presents the thermophysical properties that were used in the numerical simulations.

The finite-volume method was used to solve all transport equations (Eqns. 1-4). The *van Leer* interpolation scheme was used for the discretization of all advective terms and a linear interpolation scheme for all diffusion terms in the system of differential partial equations. For the discretization of the temporal terms, an implicit Euler scheme was used. The PISO algorithm with two correctors was used for the velocity-pressure coupling with two non-orthogonal iterations. The numerical solver, “macroS3D”, uses an iterative procedure to couple the averaged enthalpy, the liquid averaged concentration and liquid fraction on each time step.

4. Results and discussion

4.1. Furnace thermal protocol: Temperature field and heat transfer

The buoyancy driven flow is induced by temperature and concentration gradients in the liquid. In the directional solidification furnace the axial

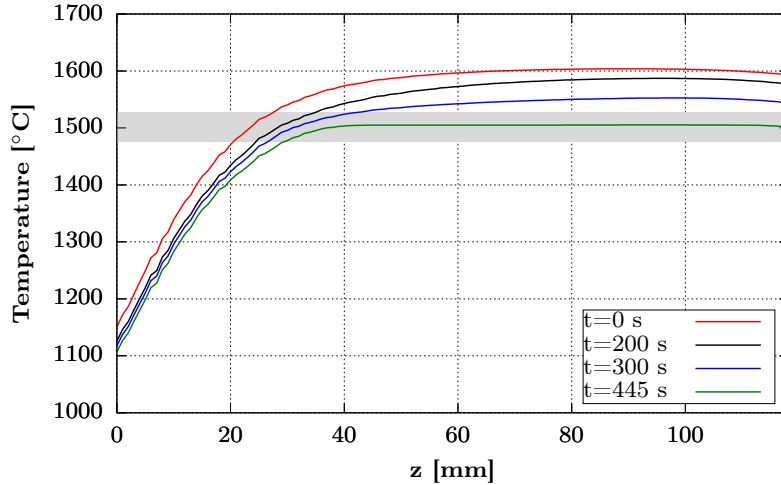


Figure 5: Example of temperature boundary condition imposed along the cylindrical sample for different times (as reported in ref. [11]). These temperature profiles are the result of the dedicated thermal furnace model. The gray shaded area represents the alloy solidification range.

thermal configuration is essentially hydrodynamically stable, *i.e.* the temperature gradient along the sample axis (z direction) does not trigger natural convection. However, convection is triggered by solute concentration gradients built up in the mushy zone due to solidification. In the TiAl alloys, the liquid in the mushy zone is progressively enriched in aluminum with decreasing temperature. The increase in Al concentration causes a decrease of the liquid density. A hydrodynamically unstable configuration is created if the solutal effect dominates over the thermal effect. Furthermore, convection is triggered by lateral temperature gradients due to heat transfer in the radial direction. The lateral temperature gradients are essential for the understanding of the flow structure in the sample, as will be seen in the simulation results later on.

To facilitate the analysis of the simulations, we will first examine the heat transfer in the sample. The objective is to explain how the lateral temperature gradients are established and how they vary with time and with position along the sample. Consider the heat equation (Eqn. 3) written in terms of the temperature, in a cylindrical coordinate system and neglecting any advective contribution. Axisymmetric conditions are assumed ($\frac{\partial T}{\partial \theta} = 0$ and $\frac{\partial T}{\partial r} \Big|_{r=0} = 0$):

Table 1: Thermophysical properties used in the simulations.

Property	Symbol	Units	Value
Nominal aluminum concentration	C_0	[wt%]	32.96
Partition coefficient	k_p	[-]	0.885
Melting point of the pure substance	T_f	[°C]	1975.66
Liquidus slope	m_l	[K/wt%]	-14.089
Pseudo-peritectic concentration	C_{inv}	[wt%]	35.2
Reference density	ρ	[kg/m ³]	3877.8
Kinematic viscosity	ν_l	[m ² /s]	1.65×10^{-6}
Thermal conductivity	k	[W/mK]	19.9
Solutal expansion coeff.	β_C	[wt% ⁻¹]	8.465×10^{-3}
Thermal expansion coeff.	β_T	[°C ⁻¹]	1.1785×10^{-4}
Latent heat	L_f	[J/kg]	3.62×10^5
Specific heat capacity	c_p	[J/(kgK)]	1100
Characteristic length for permeability	λ_2	[m]	6.50×10^{-5}

$$\left(1 + \frac{L_f}{c_p} \frac{\partial g_l}{\partial T}\right) \frac{\partial T}{\partial t} = \frac{k}{\rho c_p} \frac{\partial^2 T}{\partial z^2} + \frac{k}{\rho c_p} \frac{1}{r} \frac{\partial}{\partial r} \left(r \frac{\partial T}{\partial r} \right) \quad (9)$$

This equation shows that the temperature evolution at any point in the sample is affected by a contribution (variation of conduction heat flux) in the radial direction (r direction) and a contribution in the axial direction (z direction). Now consider that the temperature profile along the sample and over time is known, such that the axial and temporal contributions of Eqn. 9 can be explicitly calculated: $\mathbf{R}(t, z) = \left(1 + \frac{L_f}{c_p} \frac{\partial g_l}{\partial T}\right) \frac{\partial T}{\partial t} - \frac{k}{\rho c_p} \frac{\partial^2 T}{\partial z^2}$. It is assumed that $\mathbf{R}(t, z)$ only weakly depends on r . This gives the following expression for the radial contribution:

$$\frac{k}{\rho c_p} \left(\frac{1}{r} \frac{\partial}{\partial r} r \frac{\partial T}{\partial r} \right) = \mathbf{R}(t, z) \quad (10)$$

The solution of Eqn. 10 is given by:

$$T(r, t, z) = \frac{\rho c_p}{4k} \mathbf{R}(t, z) r^2 + T(r=0) \quad (11)$$

The relation of Eqn. 11 approximates the temperature profile in the radial direction. When $\mathbf{R}(t, z) > 0$ the cylinder centerline is colder than the cylinder sides, which means that the heat diffusion along the cylinder

occurs faster than the change of temperature in the boundaries, and when $\mathbf{R}(t, z) < 0$, it is in the other way around. The value of $\mathbf{R}(t, z)$ can be approximated assuming that the cylinder centerline ($r = 0$) follows a temperature profile similar to that imposed by the boundary conditions with only a small delay. This is realistic, since the heat diffusion time in the sample thickness $d^2 / (4k / (\rho c_p))$, where d is the sample diameter, is of the order of 3 s *i.e.* much smaller than the solidification time of the sample. Furthermore, this assumption is confirmed by the detailed study of heat transfer in the sample by Battaglioli et al. [16]. Figure 6 shows the value of $\mathbf{R}(t, z)$ along the sample for different times, which was approximated using the information of the boundary conditions. For $t = 50$ s, $\mathbf{R}(t, z) > 0$ throughout all the zone of interest (in and close to the mushy zone), meaning that the cylinder centerline cools down faster than the cylinder sides. On the other hand, for $t = 200$ s and $t = 400$ s there is a transition around $z = 50$ mm in which the cooling rate at the sides of the cylinder is faster than the heat diffusion along the sample, making the cylinder sides colder than the cylinder centerline. This behaviour is explained by the change of the cooling rate of the furnace thermal protocol during the solidification stage. The fully coupled numerical simulations of solidification predict that the temperature radial inversion occurs at around $z = 51$ mm at $t = 200$ s and $z = 38$ mm at $t = 400$ s.

A limitation of the simulation is that the thermophysical properties are assumed constant. In reality, the specific heat and the thermal conductivity of the liquid and solid vary with temperature. In order to explore the sensitivity of the heat transfer analysis to the assumed thermophysical properties, this analysis was also conducted using four different sets of properties. In two set of properties, the specific heat, c_p , was varied $\pm 25\%$ with respect to the one reported in Table 1, maintaining all the other properties unaltered. In the same way, in the two other sets, the thermal conductivity, k , was varied $\pm 50\%$. Table 2 summarizes the parameters of the sensitivity study.

Figure 7 presents the profiles of the radial heat diffusion, $\mathbf{R}(t, z)$, for $t = 200$ s and for the different sets of thermophysical properties. The profiles show that the magnitude of $\mathbf{R}(t, z)$ decreases with decreasing thermal diffusivity, $\frac{k}{\rho c_p}$. Moreover, the inversion of the radial temperature gradient takes place closer to the fully solid part of the sample as the thermal diffusivity decreases. This observations are explained recalling that $\mathbf{R}(t, z) = \left(1 + \frac{L_f}{c_p} \frac{\partial g_l}{\partial T}\right) \frac{\partial T}{\partial t} - \frac{k}{\rho c_p} \frac{\partial^2 T}{\partial z^2}$. Because $\frac{\partial^2 T}{\partial z^2} < 0$ in the studied cases, $\mathbf{R}(t, z)$ decreases with decreasing thermal diffusivity.

Table 2: Sets of thermophysical properties which vary the specific heat capacity and the thermal conductivity with respect to the reported in Table 1. In **bold** is remarked the different property with respect to Table 1.

Set name	Specific heat capacity	Thermal conductivity	Thermal diffusivity
-	c_p [J/(kgK)]	k [W/mK]	α_T
c_p+	1375 (+25%)	19.9	3.73×10^{-6} (-20%)
c_p-	825 (-25%)	19.9	6.22×10^{-6} (+33.5%)
$k+$	1100	29.85 (+50%)	6.99×10^{-6} (+50%)
$k-$	1100	9.95 (-50%)	2.33×10^{-6} (-50%)

4.2. Liquid flow

The case study presents a thermally stable configuration along the cylindrical sample, which means that the axial gradients of temperature will not trigger any liquid convection (the main temperature gradient is anti-parallel to the total apparent gravity). However, inside the mushy zone, the solutal buoyancy effect competes with the thermal buoyancy effect, since there is aluminum enriched liquid, which is lighter than the one at nominal concentration. By combining the buoyancy term of Eqn. 2 and the link between the temperature and the liquid concentration in the solid-liquid region (Eqn. 7), it can be shown that if $\beta_T + \frac{\beta_C}{m_l} < 0$ and the main temperature gradient is anti-parallel to the total apparent gravity, the destabilizing solutal effect dominates over the stabilizing thermal effect, resulting in thermosolutal liquid convection. Indeed, the aluminum enriched liquid in the mushy zone will tend to flow in an anti-parallel direction to the total apparent gravity due to the dominant solutal buoyancy effect, finding its way through the porous media that forms the mushy zone. A flow along the apparent gravity direction will be strongly affected by the Coriolis acceleration. The Coriolis acceleration pushes the fluid flow to the flight velocity or opposite to flight velocity sides of the sample if its direction is anti-parallel or parallel to the total apparent gravity, respectively. In order to make more evident the effect of the Coriolis acceleration, all the results are presented in the plane formed by the flight velocity vector, \vec{V}_{flight} , and the total apparent gravity vector, \vec{g}_{tot} (see Fig. 3). We define this plane as the main plane of study.

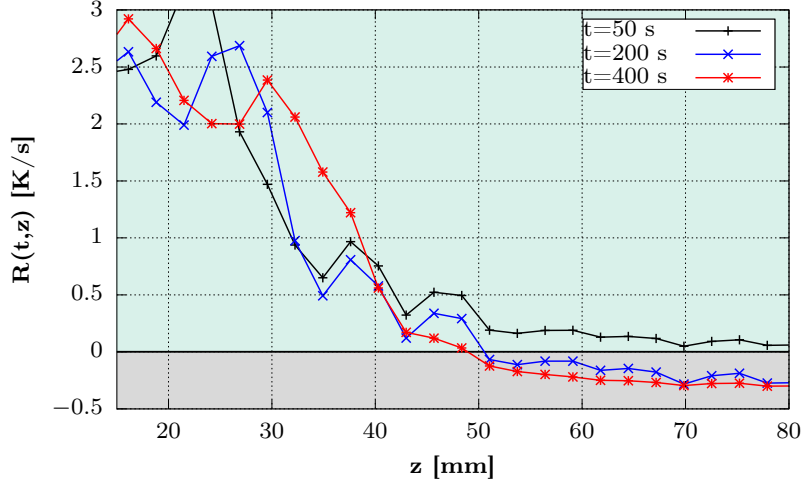


Figure 6: Contribution of the radial heat diffusion $\mathbf{R}(t, z) = \frac{k}{\rho c_p} \left(\frac{1}{r} \frac{\partial}{\partial r} r \frac{\partial T}{\partial r} \right)$. The mushy zone is located between 21 mm and 26 mm at $t = 50$ s, between 24 mm and 31 mm at $t = 200$ s and between 28 mm and 45 mm at $t = 400$ s, approximately.

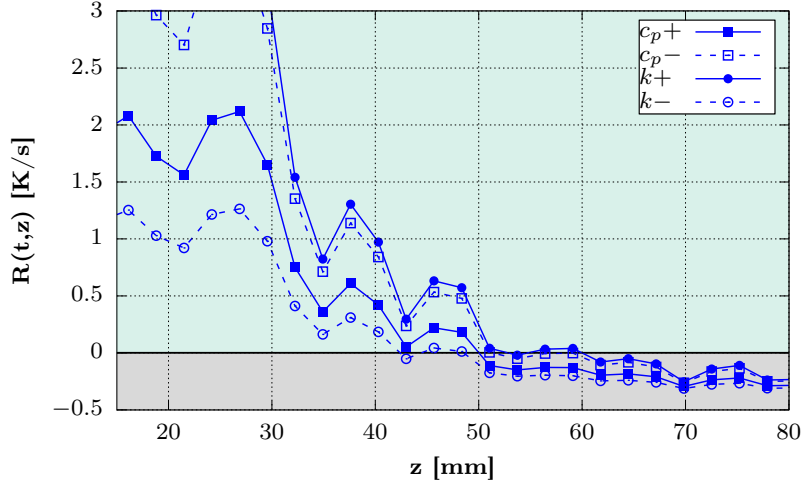


Figure 7: Contribution of the radial heat diffusion, $\mathbf{R}(t, z) = \frac{k}{\rho c_p} \left(\frac{1}{r} \frac{\partial}{\partial r} r \frac{\partial T}{\partial r} \right)$, at $t = 200$ s for the different sets of thermophysical properties (see Table 2).

4.2.1. Liquid flow in the mushy zone

Figures 8 and 9 present the liquid density, in terms of the ratio ρ_l^b/ρ , inside the mushy zone in the main plane of study for the cases 1G and 20G, respectively. Both figures show that the liquid density in the mushy zone is

lower than in the fully liquid region. This distribution is due to the aluminum enrichment in the liquid, driven by solidification.

As it was previously demonstrated, if $\mathbf{R}(t, z) > 0$, the cylinder center is colder than the cylinder sides, implying that in the radial direction solidification occurs first in the cylinder center. Along with solidification, aluminum is rejected to the liquid by the growing solid decreasing the liquid density. Indeed, in the case 1G, at $t = 50$ s and $t = 200$ s, the liquid density is lower in the cylinder center than in the cylinder sides. However, at $t = 400$ s, the inversion of the radial temperature gradient leads to a change of the liquid density configuration: for $z > 38$ mm, where $\mathbf{R}(t, z) < 0$, the lowest liquid density is located at the cylinder sides, whereas for $z < 38$ mm, where $\mathbf{R}(t, z) > 0$, the density is lower in the center. The case 20G (see Fig. 9) presents the same features as the case 1G, but with the apparition of a segregation channel, where the liquid density is lower.

Figures 10 and 11 show the liquid velocity field inside the mushy zone in the main plane of study for the cases 1G and 20G, respectively. In case 1G, for $t = 50$ s, the liquid flows along the cylinder centerline, from the fully solid region towards the fully liquid region. Before arriving to the fully liquid region, the liquid flow is deflected towards the cylinder sides where it flows returning to the fully solid region, forming a ring of three dimensional toroidal circulation. This axisymmetric flow pattern is explained due to the difference of liquid density between the center and the sides of the cylinder. A buoyancy driven flow, antiparallel to the apparent gravity, is triggered in the cylinder center due to solidification and the decrease in liquid density. This interdendritic flow, in the cylinder center, is deflected towards the cylinder sides by the action of the liquid flow in the fully region, which is parallel to the apparent gravity in the cylinder center and antiparallel in the cylinder sides (see Fig. 12). The same kind of flow pattern is also observed for $t = 200$ s but with a notable decrease of its magnitude because it is affected by the flow in the fully liquid region, which attempts to enter the mushy zone by the cylinder center. For $t = 400$ s a completely different liquid flow behaviour is observed: liquid flows towards the fully solid region in the cylinder center, while on the cylinder sides, it flows towards the fully liquid region. This change of circulation is due to the inversion of the radial temperature gradient.

On the other hand, in the case 20G, for $t = 50$ s, solute enriched liquid flows antiparallel to the apparent gravity towards the fully liquid region in the cylinder center (see Fig. 11a). The buoyancy forces, which are controlled

by solutal gradients, are strong enough to make solute enriched liquid escape from the mushy zone and enter the fully liquid region. This flow current of solute enriched liquid is deflected towards the flight velocity side of the cylinder due to the Coriolis acceleration effect. Simultaneously, liquid enters to the mushy zone by the cylinder sides to compensate the liquid that escapes from it by the cylinder center. At $t = 200$ s the solute enriched liquid flow creates a channel in the mushy zone. The channel is an elongated region where the solid fraction is lower than in the surrounding mushy zone [17]. Due to a higher permeability, the channel is a self-reinforcing preferential path for the flow. At $t = 400$ s the channel is extinct. A flow pattern similar to the one observed in the case 1G is present, however not axisymmetric due to the deflecting effect of the Coriolis acceleration.

4.2.2. Liquid flow in the fully liquid region

Figures 12 and 13 present the liquid fraction and the liquid velocity for cases 1G and 20G in the fully liquid region, respectively. In case 1G, for $t = 50$ s, liquid flows towards the solidification front in the cylinder center, whereas, in the cylinder sides, it flows antiparallel to the apparent gravity vector. At this instant, the cylinder center is colder than the sides. The flow pattern is explained by thermal buoyancy which is the dominant driving force for the flow in the fully liquid region. For $t = 200$ s and $t = 400$ s, the flow evolves with the temperature field which is controlled by the boundary conditions. For example, at $t = 200$ s in the zone $z > 60$ mm, the liquid flows antiparallel to the apparent gravity in the cylinder center, whereas, it flows parallel in the cylinder sides and for $z < 60$ mm, the flow is in the other way around. This behaviour is explained due to the radial inversion of the temperature gradient (recall the analysis of the furnace thermal protocol and temperature field).

In case 20G, the aluminum enriched liquid that escapes from the mushy zone due to the strong solutal buoyancy effect, is deflected by the Coriolis acceleration to the flight velocity side of the cylinder. This liquid advances all along the sample by the flight velocity side and returns to the mushy zone by the opposite to flight velocity side forming a large clockwise circulation (see Fig. 13). This large circulation is present in all the studied cases with centrifugation and makes the fluid flow pattern entirely non-axisymmetric. Indeed, the solutal buoyancy effect along the cylinder is stronger than the stabilizing thermal effect and the radial thermal gradients induced by the furnace thermal protocol do not play a role in determining the fluid flow

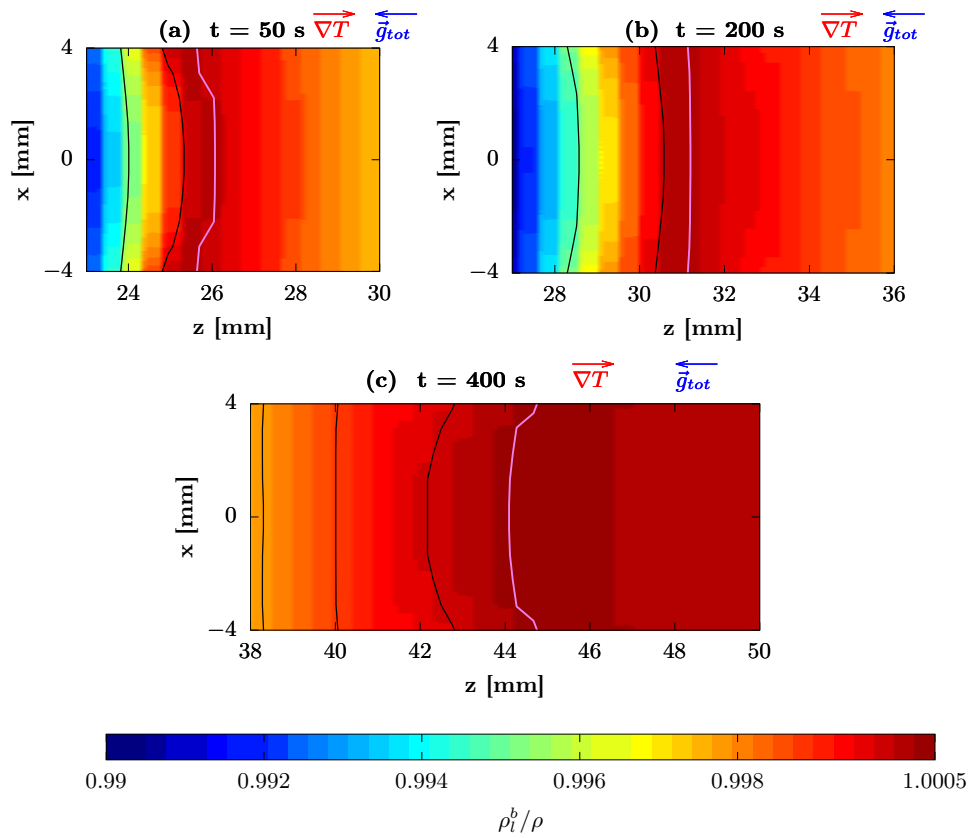


Figure 8: Evolution of the liquid density, in terms of ρ_i^b/ρ in the main plane of study within the mushy zone for the case 1G. Violet contours delimit the mushy zone. For (a) and (b), temperature contours in black: 1500, 1510 °C. For (c) temperature contours 1506, 1508 and 1510 °C.

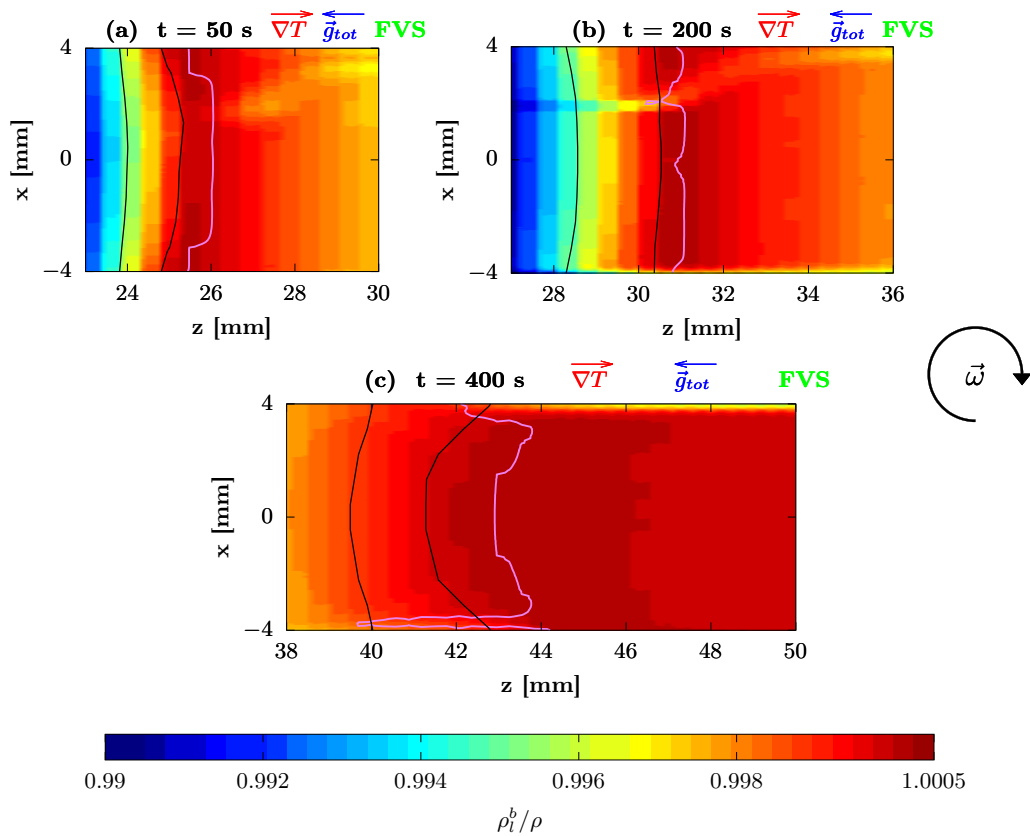


Figure 9: Evolution of the liquid velocity and liquid fraction in the main plane of study within the mushy zone for the case 20G. *FVS* denotes the flight velocity side of the sample. Violet contours delimit the mushy zone. For (a) and (b), temperature contours in black: 1500 and 1510 °C. For (c) temperature contours 1508 and 1510 °C.

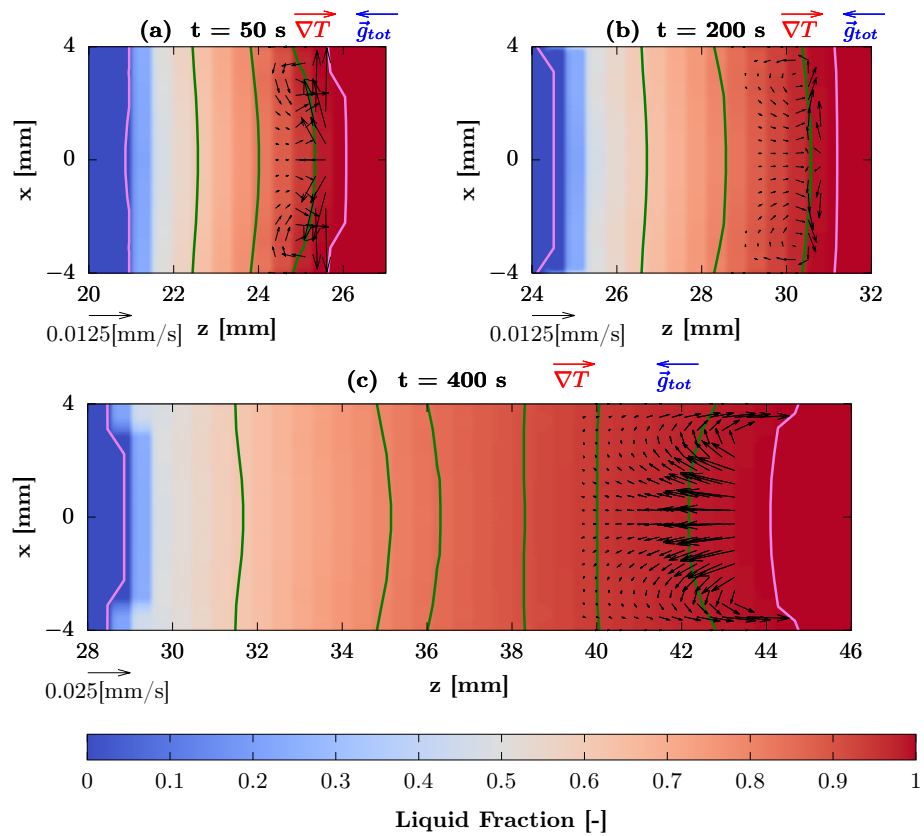


Figure 10: Evolution of the liquid velocity and liquid fraction in the main plane of study inside the mushy zone for the case 1G. Violet contours delimit the mushy zone. For (a) and (b), temperature contours in green: 1490, 1500 and 1510 °C. For (c) temperature contours 1490, 1500, 1503, 1506, 1508 and 1510 °C.

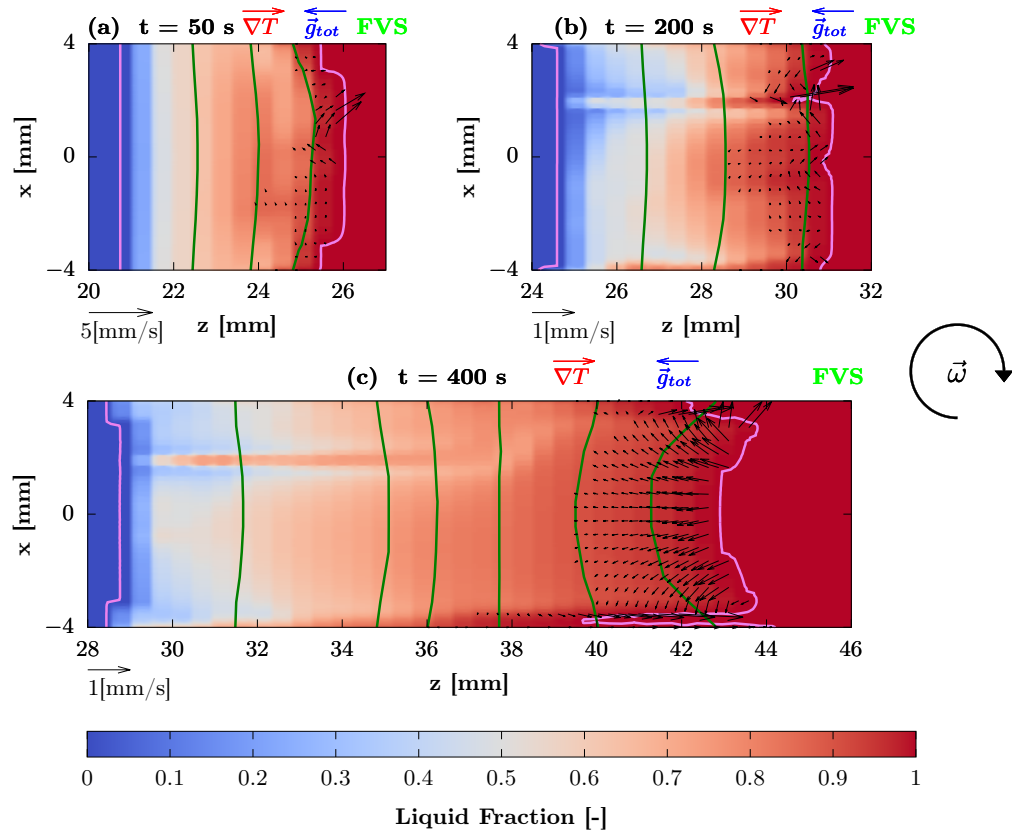


Figure 11: Evolution of the liquid velocity and liquid fraction in the main plane of study in the mushy zone for the case 20G. *FVS* denotes the flight velocity side of the sample. Violet contours delimit the mushy zone. For (a) and (b), temperature contours in green: 1490, 1500 and 1510 °C. For (c) temperature contours 1490, 1500, 1503, 1505.2, 1508 and 1510 °C.

pattern (as they do in case 1G).

To distinguish the thermal and solutal effects on the liquid convection in the fully liquid region, Figures 14 and 15 present the liquid density, in terms of ρ_l^b/ρ , along with the temperature and the average solute concentration in the liquid at $t = 200$ s for the cases 1G and 20G, respectively. We should keep in mind that the temperature fields in both cases are virtually identical (see Fig. 14a and 15a) because they are mainly controlled by the boundary conditions. In case 1G, the solute enriched liquid is retained in the mushy zone by the liquid flow in the fully liquid region. As a result, there are no significant concentration gradients in the fully liquid zone. The liquid density in the fully liquid zone is controlled only by the thermal effect, leading to a stable configuration. The convection in this zone is therefore driven exclusively by radial temperature gradients. On the other hand, in the 20G case, solute enriched liquid escapes from the mushy zone in a stream that is anti-parallel to the apparent gravity and is therefore pushed to the flight velocity side by the Coriolis acceleration (see Fig. 15b). The liquid density map clearly shows that the lightest liquid is located along the flight velocity side. It is concluded that the convection in fully liquid zone is driven by solutal buoyancy forces in the 20G case and by thermal buoyancy forces in the 1G case.

Müller et al. [5] and later Ramachandran et al. [6] described two types of flow regime in cases of thermally driven convection within cylindrical samples submitted to centrifugation. The descriptions are based on the fluid flow pattern in the plane perpendicular to the rotation axis. The first regime, or regime type I, consists of a single dominant circulation whose rotation is counter sense with respect to the rotation of the centrifuge. In addition, this type of regime presents eddy currents in the corners of the container that cause an unsteady behaviour of the flow pattern. On the other hand, the regime type II consists in a single dominant circulation whose rotation sense is the same than the one of the centrifuge. The second type of regime is completely dominated by the influence of the Coriolis acceleration.

In order to establish the impact of the Coriolis acceleration on the determination of the fluid flow features, we investigated the Rossby dimensionless number. The Rossby number is the ratio between the inertia and the Coriolis accelerations and can be defined as $Ro = \frac{U_{ref}}{2\omega L}$, where U_{ref} is a reference velocity, ω the magnitude of the centrifuge angular velocity and L a characteristic length. The reference velocity U_{ref} was considered as the average of the maximum velocity at the instants $t = 50$ s, $t = 200$ s and $t = 400$ s in the main plane of study. The characteristic length was considered to be

Table 3: Total apparent gravity (g is the normal terrestrial gravity), centrifuge angular velocity, ω , reference velocity, U_{ref} and Rossby number, $Ro = \frac{U_{ref}}{2\omega L}$ for all the studied cases. The reference velocity is considered to be the average of the maximum velocity in the main plane of study at the instants $t = 50$ s, $t = 200$ s and $t = 400$ s.

Case	g-level	ω [rad/s]	U_{ref} [mm/s]	Ro [-]
1G	1g	0.00	0.13	∞
5G	5g	3.47	2.13	3.06×10^{-3}
10G	10g	4.94	3.58	3.62×10^{-3}
15G	15g	6.06	4.77	3.94×10^{-3}
20G	20g	7.00	7.67	5.48×10^{-3}

$L \sim 100$ mm, which is the approximate length of the fully liquid region at $t = 50$ s. Table 3 presents the reference velocity, U_{ref} , the centrifuge angular velocity, ω , and the Rossby number, Ro , for each one of the investigated cases. The numerical results shows that in all the cases with centrifugation, $Ro \ll 1$, which means that the Coriolis acceleration is very important in determining the fluid flow features. According to the descriptions of Müller et al. and Ramachandran et al., the flow regime in the fully liquid region corresponds to type II in all the studied cases with centrifugation.

Figure 16 shows three-dimensional views of the domain during solidification at $t = 150$ s for the relative solute segregation and axial velocity magnitude in the case 20G. It can be seen that in the fully liquid region, solute enriched liquid is located in the flight velocity side of the sample due to the combined effect of the centrifugal and Coriolis accelerations. The unique large liquid circulation and the non-axisymmetric liquid flow is clearly noticeable.

4.3. Aluminum macrosegregation

Macrosegregation is the heterogeneity in solute composition – in this case aluminum – at the macroscopic scale due to the relative movement of the solid and liquid phases during a solidification process. By combining Eqns. 4 and 7 it can be shown that the average concentration, $\langle C \rangle$, in any point in the mushy zone varies as $\frac{\partial \langle C \rangle}{\partial t} = -\frac{1}{m_l} g_l \langle \vec{v}_l \rangle^l \cdot \nabla T$. This is a useful relation to understand the macrosegregation patterns due to liquid movement in the absence of density variations (shrinkage) and solid deformations. Note that $m_l < 0$.

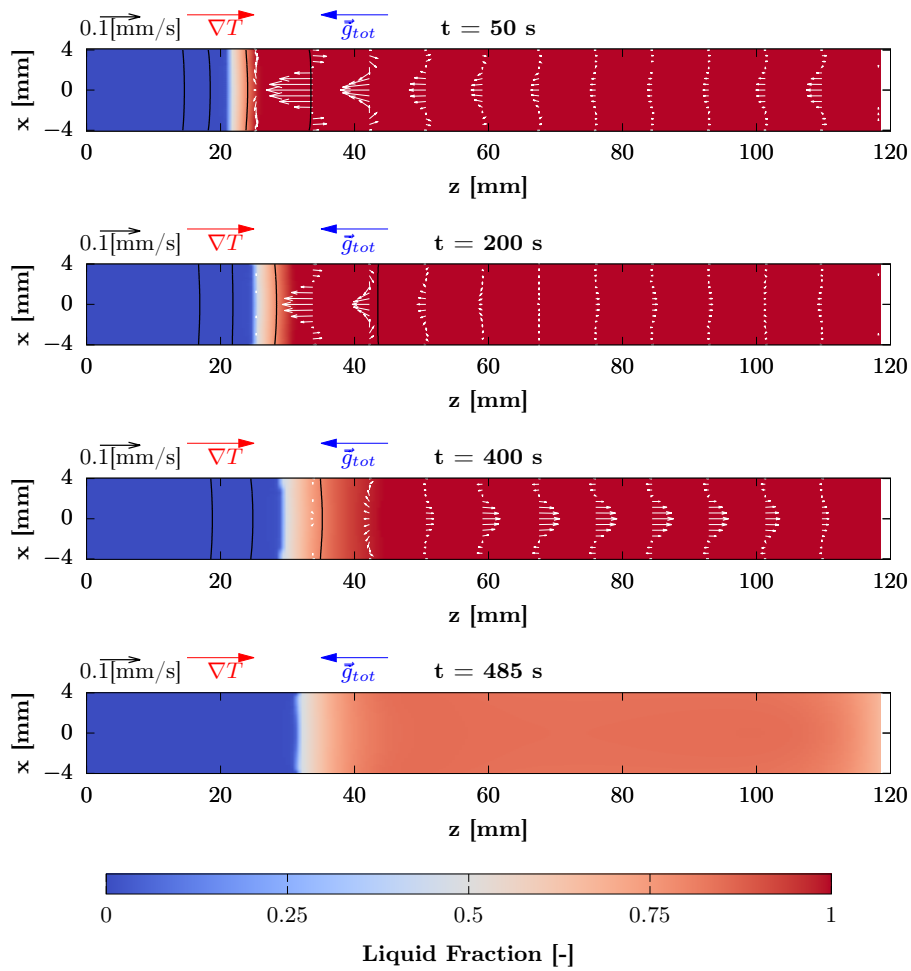


Figure 12: Evolution of the liquid velocity pattern in the main plane of study in the fully liquid region for the case 1G. Temperature contours in black: 1400, 1450, 1500 and 1550 °C.

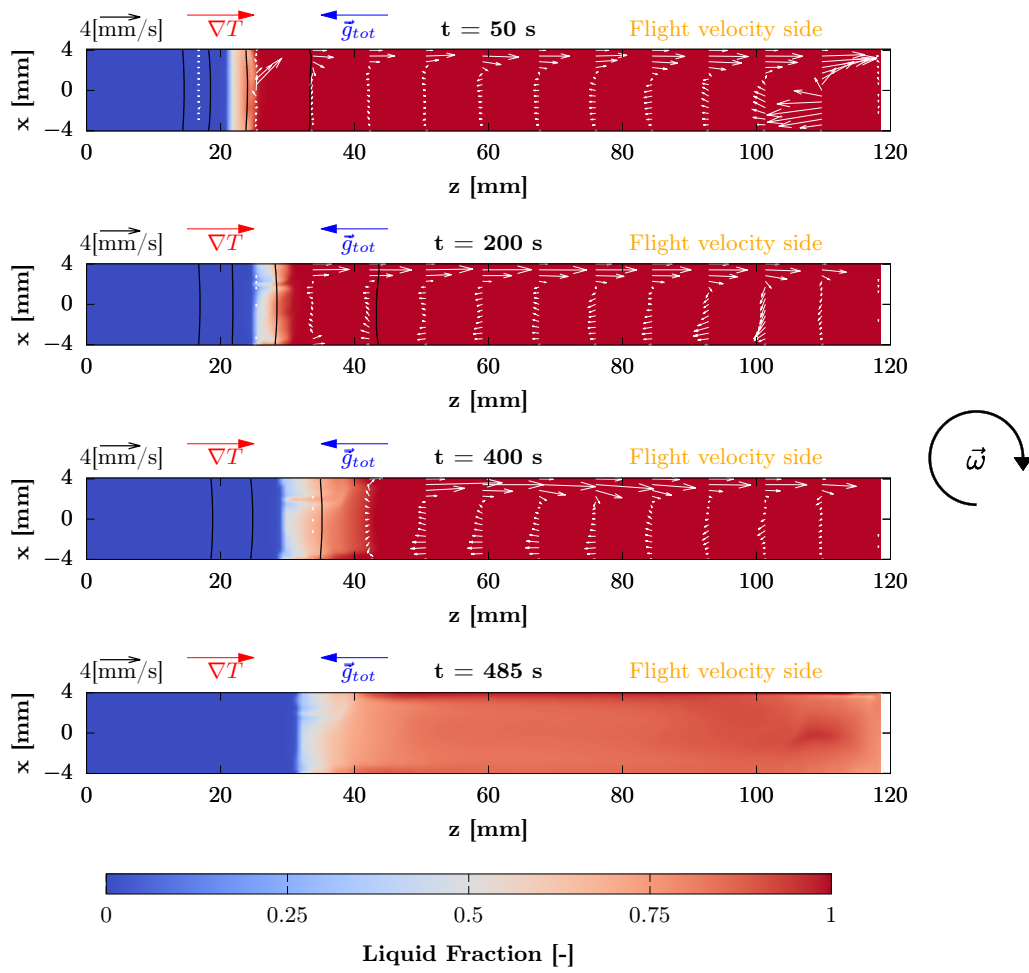


Figure 13: Evolution of the liquid velocity pattern in the main plane of study in the fully liquid region for the case 20G. Temperature contours in black: 1400, 1450, 1500 and 1550 °C.

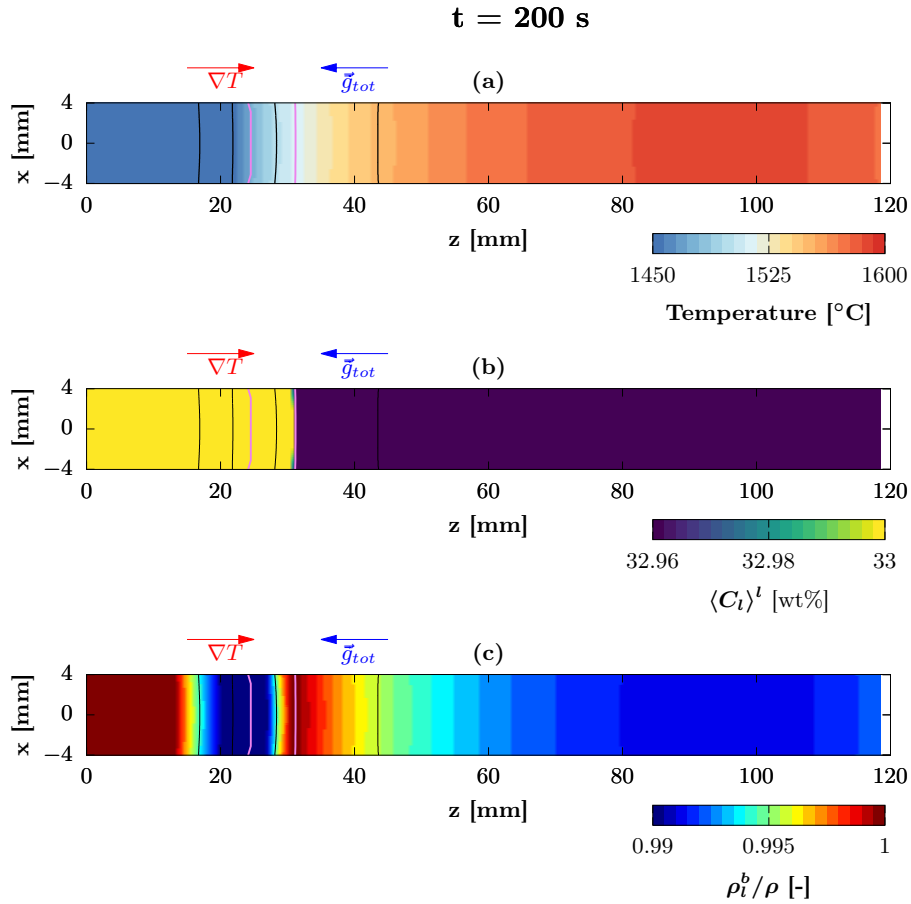


Figure 14: Temperature, average concentration in the liquid and liquid density (in terms of ρ_i^b / ρ) in the main plane of study at $t = 200$ s for the case 1G. Violet contours delimit the mushy zone. Temperature contours in black: 1400, 1450, 1500 and 1550 °C.

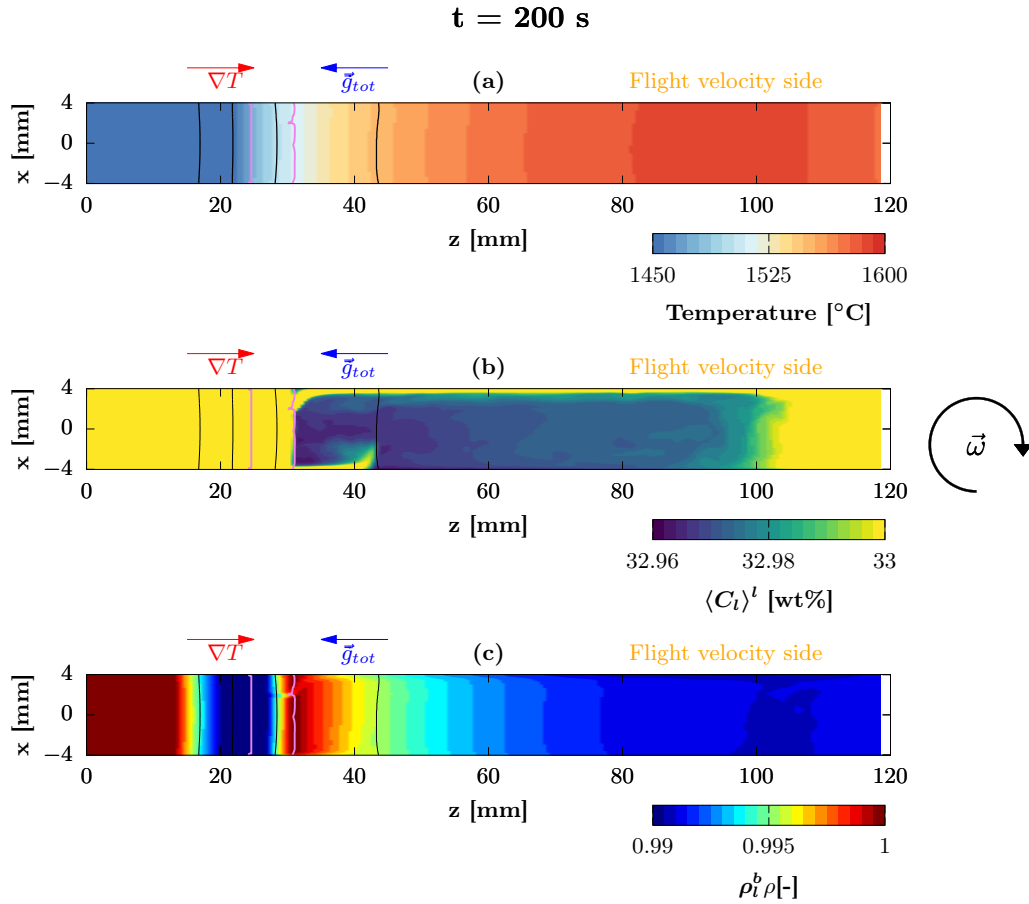


Figure 15: Temperature, average concentration in the liquid and liquid density (in terms of ρ_l^b / ρ) in the main plane of study at $t = 200 \text{ s}$ for the case 20G. Violet contours delimit the mushy zone. Temperature contours in black: 1400, 1450, 1500 and 1550 °C.

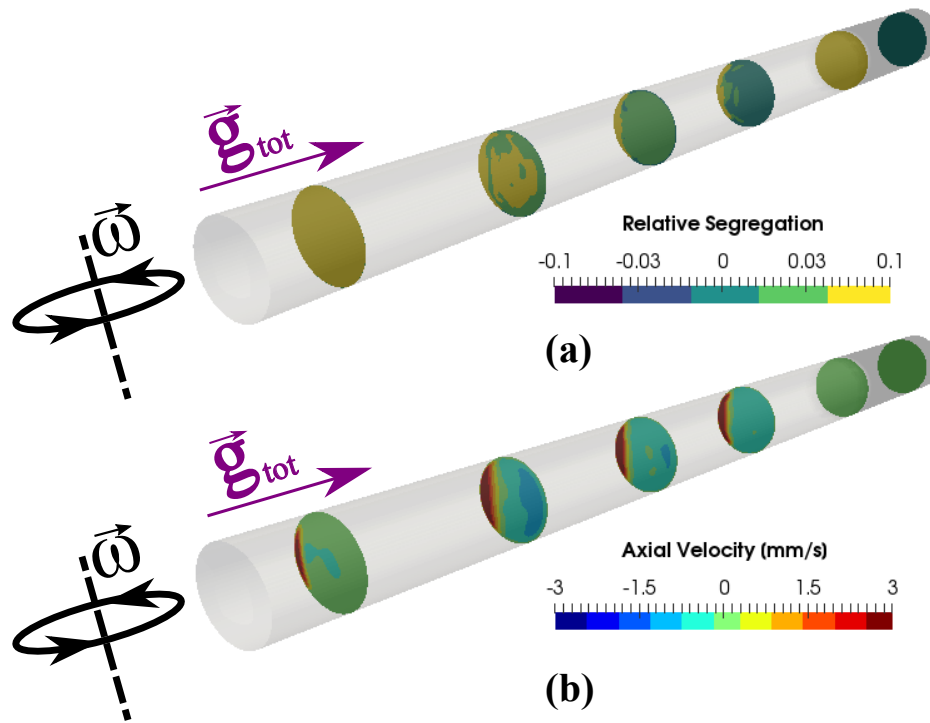


Figure 16: 3D views of the domain at $t = 150$ s for the case 20G. (a) Relative segregation $\frac{\langle C \rangle - C_0}{C_0} \times 100\%$. (b) Axial intrinsic liquid velocity magnitude (negative magnitude in the direction parallel to the apparent gravity).

Figure 17 shows the aluminum relative segregation in the main plane of study for the different cases at the end of solidification. In case 1G, the overall relative segregation is axisymmetric such as the thermosoultal liquid convection and its maximum magnitude is around 0.29%. This weak magnitude of segregation can be explained mainly by: (1) the large partition coefficient, $k_p = 0.885$, close to unity, meaning that the aluminum concentration in liquid and solid phases is similar (recall $\langle C_s \rangle^s = k_p \langle C_l \rangle^l$), and (2) the weak liquid convection with respect to the cases with centrifugation. Along the sample, three different segregation patterns can be easily identified. For $20 \text{ mm} \leq z \leq 40 \text{ mm}$ a negative segregation is present in the cylinder sides whereas positive in the cylinder centerline. This pattern is explained since the liquid flow is parallel to the main temperature gradient ($\langle \vec{v}_l \rangle^l \cdot \nabla T > 0$) along the sample in the cylinder centerline, bringing solute enriched liquid from deep in the mushy zone to the solidification front, and anti-parallel ($\langle \vec{v}_l \rangle^l \cdot \nabla T < 0$) in the cylinder sides, taking poor liquid in solute from the solidification front to deep in the mushy zone (see Fig. 10[a,b]). On the other hand, for $40 \text{ mm} \leq z \leq 95 \text{ mm}$ the segregation pattern is in the other way around: positively segregated in the cylinder sides, whereas negatively in the cylinder center. This pattern is explained by the inversion of the flow direction (see Fig. 10c). The same liquid flow pattern is observed for $z \geq 95 \text{ mm}$, however, there is a second solidification front moving from the other end of the sample parallel to the apparent gravity vector (for $t > 400 \text{ s}$), enriching in solute the center of the cylinder and depleting its sides. It is worth to mention that according to the furnace thermal protocol, the zone $z > 40 \text{ mm}$ solidifies very fast and at $t = 487 \text{ s}$ the sample is fully quenched.

In cases with centrifugation, we observe that the segregation pattern is not axisymmetric due to the deflecting effect of the Coriolis acceleration on the liquid convection. Such as in the case 1G, we recognize the same three zones, however with important differences in the segregation pattern. The first zone between $20 \text{ mm} \leq z \leq 40 \text{ mm}$ presents a similar pattern to the case 1G, but more strongly segregated, non-axisymmetric and with the occurrence of segregation channels (see 10G and 20G cases in Fig. 17). The second zone $40 \text{ mm} \leq z \leq 95 \text{ mm}$ has a positive segregation in in the cylinder sides, with a more strongly aluminum enriched zone in the flight velocity side. This feature is due to the deflecting effect of the Coriolis acceleration. The third zone, $z > 95 \text{ mm}$, it is almost fully positively segregated (some small negatively segregated zones can be seen in the 5G case at the cylinder sides) because of

the accumulation of light aluminum enriched liquid. Finally, the aluminum segregation pattern in cases with centrifugation is not greatly influenced by the furnace thermal protocol, due to the liquid convection is entirely driven by buoyancy solutal forces.

Figure 18 presents the relative aluminum segregation in three transversal planes for the 15G case. We can notice localized positive segregation in spots distributed around the sample circumference. They are a consequence of instabilities at the cylinder sides that do not evolve into fully developed channels. These instabilities appear in the cylinder in the beginning of the temperature radial inversion that has been described previously. The occurrence of such instabilities can be sensitive even to minor variations in the temperature field. As discussed in Section 4.1, these can be triggered by varying thermophysical properties. Varying the thermophysical properties implies a variation of the magnitude of the radial heat diffusion and of the position of the radial temperature gradient inversion (see Fig. 7). This also implies that the axial position, where the positively segregated spots appear, varies according to the position of the radial temperature gradient inversion, *i.e.* the positively segregated spots appear earlier in the domain if the thermal diffusivity is smaller. The simulations show that the solute enrichment intensity and quantity of the spots increases as the thermal diffusivity decreases (not shown here). To illustrate this effect, Figure 19 shows a comparison of the transversal segregation profile for the case 15G (plane $z = 35$ mm) between two sets of thermophysical properties: (1) $k+$ and (2) $k-$ (see Table 2). In the figure, ten spots are recognized when the set $k-$ is used, whereas only five in case of set $k+$. Note that the segregation intensity within the spots is larger in case of the set $k-$.

Finally, it is worth to mention that extensive numerical studies [18] have shown that the exact quantity, position and intensity of such segregation spots is extremely difficult, and perhaps even impossible, to predict with macroscopic models of solidification.

5. Comparison to aluminum measurements

In order to validate our observations with respect to the one-vortex fluid flow pattern which develops in the cases with centrifugation, measurements of aluminum concentration were made in the sample solidified with an apparent gravity of $\vec{g}_{tot} = 15g$ (15G case). Three lines along the cylindrical sample, in the main plane of study, were selected to conduct the measurements: One

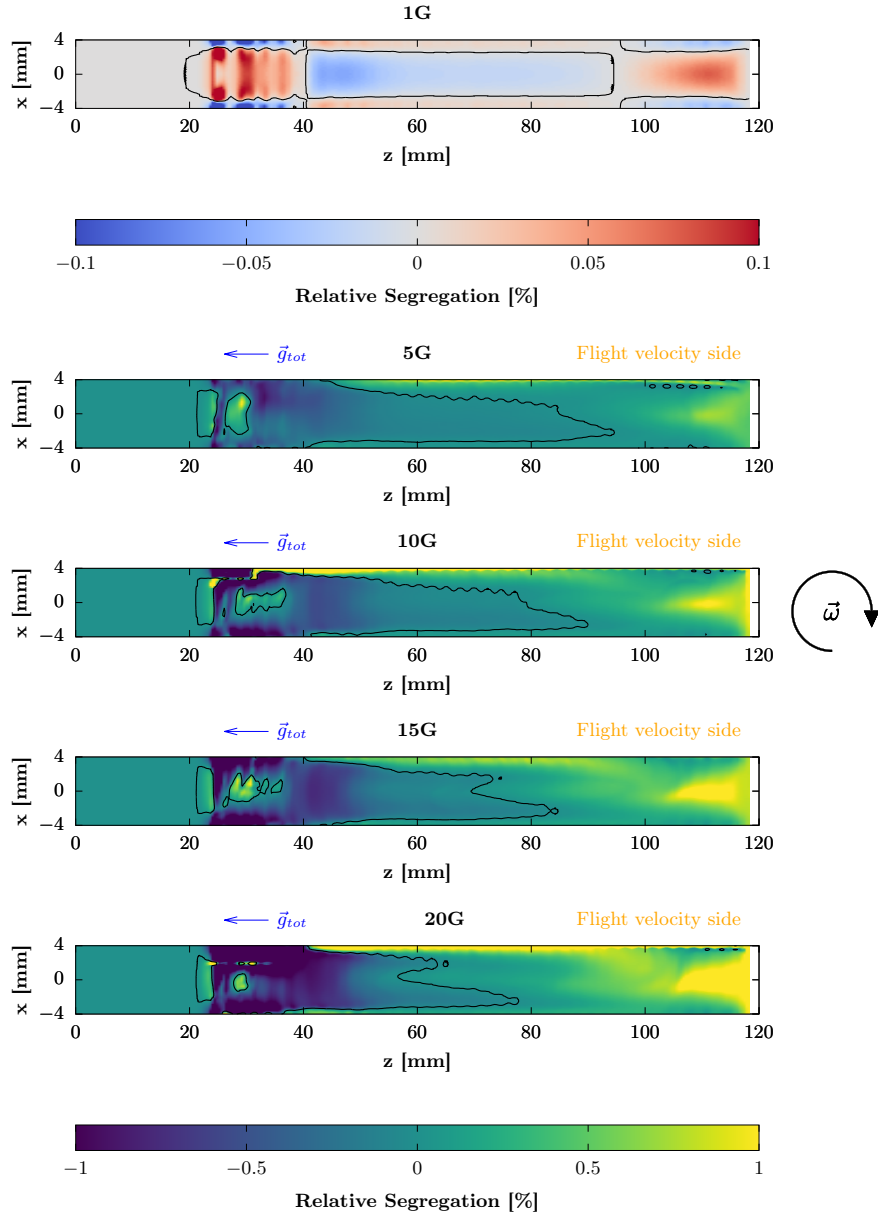


Figure 17: Relative aluminum segregation $\frac{\langle C \rangle - C_0}{C_0} \times 100\%$ in the main plane of study at the end of solidification for different centrifugation levels. Contours at $\langle C \rangle = C_0$ (black line).

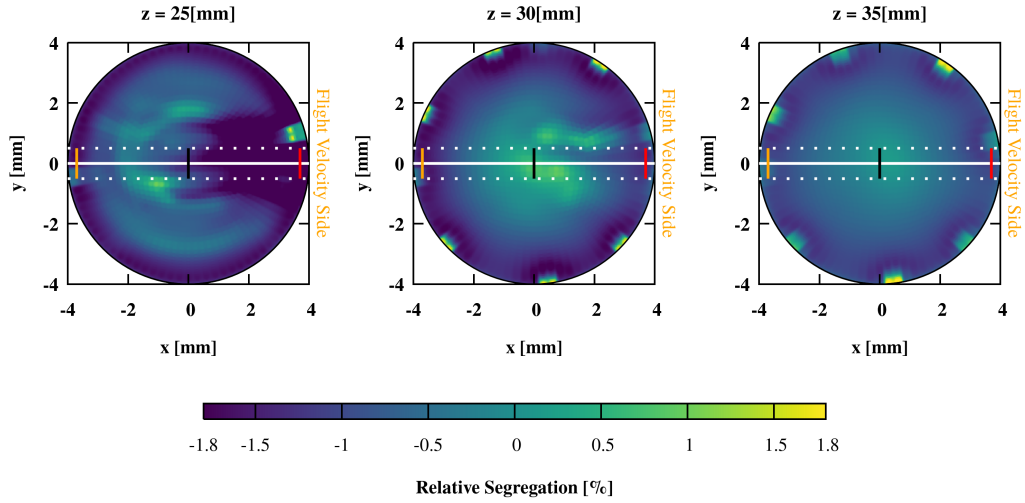


Figure 18: Relative segregation $\frac{\langle C \rangle - C_0}{C_0} \times 100\%$ for the case 15G in transversal planes at the end of solidification.

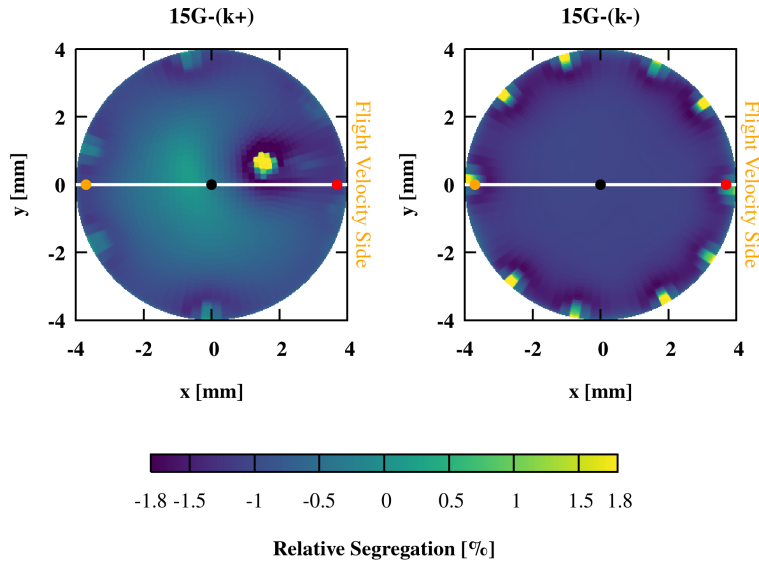


Figure 19: Relative segregation, $\frac{\langle C \rangle - C_0}{C_0} \times 100\%$, in the transversal plane $z = 35\text{[mm]}$. The white line represent the projection of the main plane of study. The points orange, black and red represent the segregation sampling position of the axial lines for Figure 20.

line in the cylinder centerline and two in the periphery (flight direction side and opposite to flight direction side). Each measurement line started at $z = 21$ mm covering a length of 40 mm (in total, 81 EDX measurement were performed).

Figure 20 presents the comparison between the results of the aluminum composition obtained by means of numerical simulations and experimental measurements. A three-point moving average smoothing of the experimental profiles was used to improve the visualization and interpretation of the measurements. The figure also presents dashed lines that were sampled 0.5 mm and -0.5 mm displaced along the y -axis direction (normal to the main plane of study) from numerical simulation results. This allow us to realize how much can change the aluminum composition slightly displacing the sampling line position in an unstable mushy zone. It is worth to mention that in the centrifugally solidified sample, the columnar-to-equiaxed transition was present around $z = 35$ mm. Any interpretation comparing the numerical results with the measurements for $z \geq 35$ mm should be done considering that the model is only valid for motionless solid (columnar growth or after packing of all equiaxed grains). The numerical profiles obtained using the set of thermophysical properties $k+$ (magenta line) and $k-$ (blue line) are also shown. The segregation profiles that correspond to the other sets of thermophysical properties are not shown because they present a very weak sensitivity to the variation of the specific heat parameter. Figure 18 schematizes with a solid white line the main plane of study, with dashed-white-lines the planes displaced ± 0.5 mm along the y -axis direction and with orange (opposite to flight direction side), black (cylinder centerline) and red (flight direction side) lines the localization of numerical sampling points in transversal planes. In the same way, Figure 19 schematizes with orange, black and red points the localization of the sampling points in case of using the sets of thermophysical properties $k+$ and $k-$.

The numerical simulation of the 15G case is able to depict the segregation of aluminum in the axial direction and gives a good qualitative match to the measurements in the centerline and in the opposite to flight velocity side. However, the flight velocity side presents a strong positive segregation throughout all the investigated length, feature that was underestimated by the numerical model. The case 15G-($k-$) presents an strong enrichment earlier than the other cases because the profile was sampled inside of one of the numerous positively segregated spots as shown in Fig. 19.

The numerical model could depict the entirely non-axisymmetric ther-

mosolutal liquid convection with the unique large circulation (type II according to the descriptions of Müller et al. [5]). This can be confirmed since the flight velocity side of the sample is notoriously more enriched in aluminum than the opposite to flight velocity side due to the deflecting effect of the Coriolis acceleration. In spite of the good agreement in depicting the fluid flow convection pattern, the numerical model could not quantitatively predict the magnitude of aluminum segregation. The quantitative prediction of flow and segregation could be very sensitive to the employed microscopic grain growth kinetics model, the assumed microstructure, the assumed pseudo-binary alloy, the assumed thermophysical properties of the material and the temperature field, especially in the radial direction. This aspect of modeling of the experiment should be refined, to achieve quantitative simulations.

6. Conclusions

In this work the application of a numerical model to predict liquid thermosolutal convection and aluminum macrosegregation during centrifugal casting of TiAl alloy was performed. The results of this study allows us to understand in a better way the deflecting effect of the Coriolis acceleration in the GRADECET experiments, where the temperature and solute gradients play an important role in the buoyancy driven convection. The general remarks can be summarized as follows:

- In spite of the axial thermally stable configuration, where the main temperature gradient is anti-parallel to the apparent gravity, TiAl alloys present an unstable mushy zone since the solutal effect counteracts the thermal effect.
- The temperature field behaviour was characterized. Special attention was paid to the inversion of the radial temperature gradient imposed by the furnace thermal protocol.
- The furnace protocol could have an impact on the liquid thermosolutal convection and on aluminum macrosegregation in the 1G case. The fluid flow pattern was mainly dependent on the ratio between the thermal diffusion along the sample and the cooling rate from the sides. In cases with centrifugation, the solutal effect on the buoyancy driven flow is much stronger than the thermal effect imposed by the radial temperature gradients.

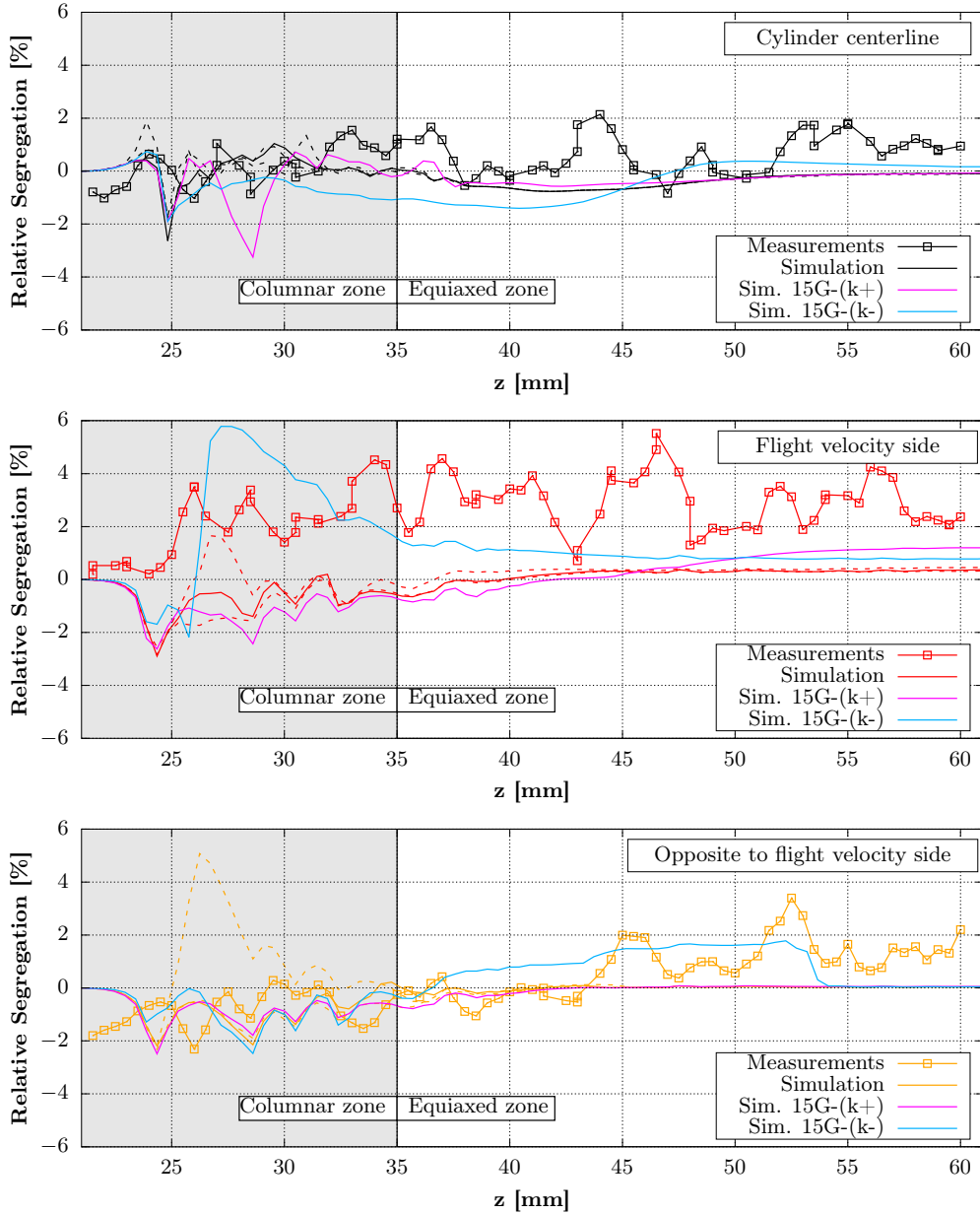


Figure 20: Comparison of aluminum concentration between EDX measurements and numerical simulation for the case 15G. Line-point: Measurements (3-point moving averaging). Solid Line: Numerical results. Dashed line: Numerical results displaced 0.5 mm and -0.5 mm in the y -axis direction (normal to the main plane of study). The blue line represent the simulation with the set of properties $k-$, whereas the magenta line with the set of properties $k+$. The columnar and equiaxed zone are delimited according to the grain morphology characterizations performed on post-mortem 15G sample of the GRADECET experiments [8].

- The Rossby number for all the studied cases with centrifugation is much smaller than unity. For these cases, the Coriolis effect determines completely the fluid flow pattern.
- The Coriolis effect pushes the lighter liquid to the flight velocity of the sample, generating one large circulation throughout the fully liquid region. This is in agreement with previous observations (Müller et al. [5] and Ramachandran [6]).
- A comparison between aluminum concentration measurements and simulation results on the case 15G was performed. The numerical model could depict qualitatively the aluminum segregation pattern and the fluid flow features. However, a quantitative prediction of the aluminum segregation magnitude could not be achieved.
- A higher aluminum concentration is present in the flight velocity side with respect to the opposite to flight velocity side of the samples centrifugally solidified. This is due to the thermosolutal convection that is modified by the deflecting effect of the Coriolis acceleration.
- The sensitivity of the results to the use of different sets of thermophysical properties was explored. It was concluded that when the thermal diffusivity decreases, the inversion of the radial temperature gradient takes place closer to the fully solid region of the sample. In addition, a lower thermal diffusivity enhances the magnitude of the instabilities in the mushy zone when the inversion of the radial temperature gradient takes place.

Improvements of the numerical model regarding to a more physical solid growth description, grain movement and columnar-to-equiaxed representation are perspective work to be made in order to improve the understanding of the GRADECET experiments.

Appendix A. Mesh sensitivity analysis

An important aspect that may introduce variations on the predicted liquid flow, and thus, on the predicted aluminum segregation, is the employed spatial discretization or mesh. In order to understand the impact that the spatial discretization can have on the results, four additional simulations of

Table A.4: Number of cells along the cylinder length and along the cylinder diameter for the different meshes employed for studying mesh sensitivity. The number of cells along the diameter corresponds to the its averaged value.

Case	Number of cells		
	Total	Length	Diameter
M0	9.37×10^5	300	55.9
Ref	5.00×10^5	250	44.7
M1	2.25×10^5	200	33.5
M2	1.08×10^5	150	26.8
M3	3.20×10^4	100	17.9

the case 15G were performed using different mesh size. In these new simulations the meshes were structured in the same way as the preceding sections (Sections 3 and 4). This means that all the meshes were constituted by hexahedral cells distributed following a *O-H grid* in the cylindrical geometry. Here, the assumed thermophysical properties were as reported in Table 1. Figure A.21 shows transversal planes of different meshes utilized in these new simulations. The figure also shows the *Reference* mesh that was already used in the preceding sections. In Table A.4 is reported information about the number of cells along the cylinder length and along the cylinder diameter for the different meshes.

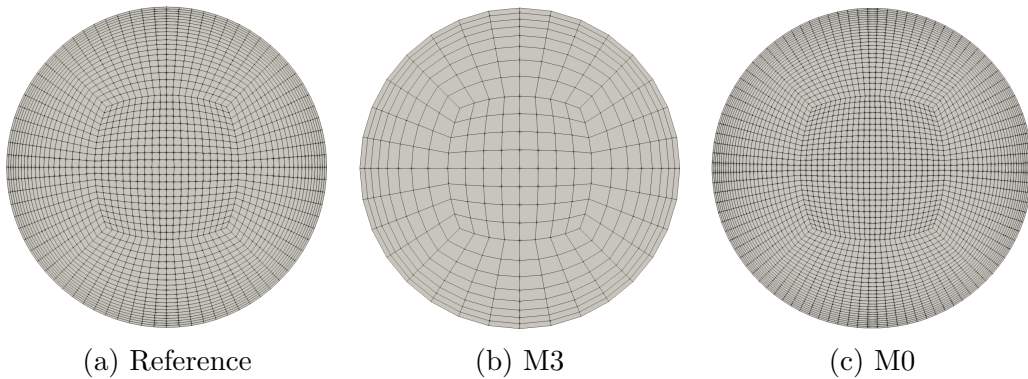


Figure A.21: Transversal planes that reveal the mesh size utilized for some of the simulations to study mesh sensitivity. The *Reference* mesh corresponds to the one used in the previous sections. The number of cells along the cylinder length and along the cylinder diameter are reported in Table A.4.

In order to have a global picture of the effect of the mesh on the results, the final aluminum segregation pattern in the main plane of study for the case 15G is shown in Figure A.22. The figure can be compared also to the segregation pattern of the 15G case shown in Figure 17. Comparing the results obtained with different meshes, it can be concluded that they do not converge to a unique solution as the mesh is refined. In spite of the different solutions, all the simulations show the same qualitative features and the same order of magnitude of the different physical quantities (liquid fraction, liquid velocity, solute concentration, etc.). These observations regarding the mesh sensitivity have been previously pointed out by Combeau et al. [18]. They concluded – using a macroscopic model for solidification very similar to the one used in this work – that in an unstable configuration of mushy zone, the position, the segregation intensity and the size of the numerically predicted segregation channels is very sensitive to the numerical method, numerical scheme and mesh.

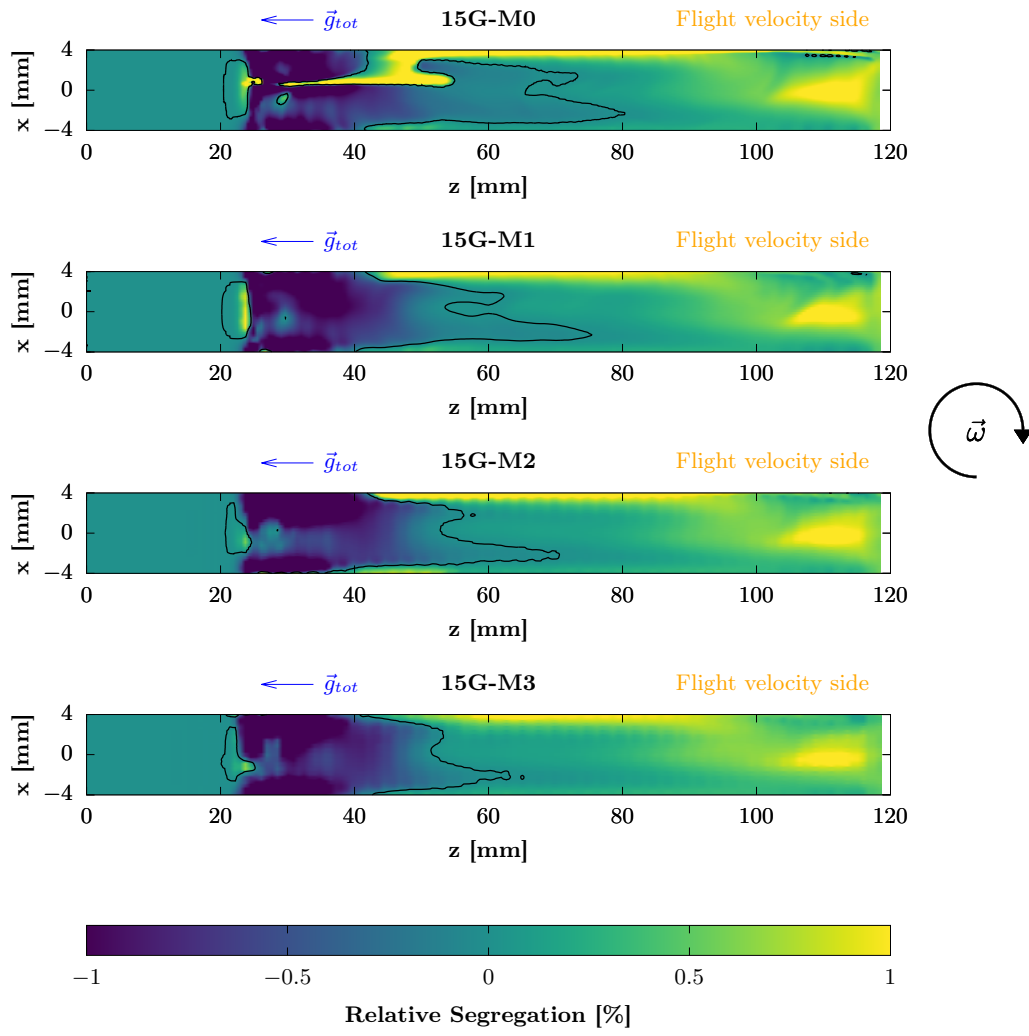


Figure A.22: Relative aluminum segregation $\frac{\langle C \rangle - C_0}{C_0} \times 100\%$ in the main plane of study at the end of solidification for the case 15G using different meshes (see Table A.4). Contours at $\langle C \rangle = C_0$.

Appendix B. Nomenclature

$\langle C \rangle$	Averaged solute concentration
C_{inv}	Pseudo-peritectic concentration
C_{ref}	Reference concentration
C_0	Nominal composition
$\langle C_j \rangle^j$	Averaged solute concentration of phase j
c_p	Specific heat
g_l	Liquid fraction
g	Normal terrestrial gravity
\vec{g}_{tot}	Total apparent gravity (sum of centrifugal acceleration and the terrestrial gravity)
$\langle h \rangle$	Averaged specific enthalpy
k	Thermal conductivity
K	Hydrodynamic permeability
k_p	Partition coefficient
L_f	Latent heat
L	Characteristic length
m_l	Liquidus slope
p	Pressure
$\mathbf{R}(t, z)$	Contribution of radial heat diffusion
Ro	Rossby number
T	Temperature
T_f	Melting point of the pure substance
T_{per}	Peritectic temperature
U_{ref}	Reference velocity
\vec{V}_{flight}	Flight velocity vector
$\langle \vec{v}_j \rangle^j$	Averaged intrinsic velocity of phase j
ν_l	Kinematic liquid viscosity
ρ	Reference density
ρ_l^b	Buoyant liquid density
β_C	Thermal expansion coefficient
β_C	Solutal expansion coefficient
$\vec{\omega}$	Centrifuge angular velocity
λ_2	Characteristic length for permeability, secondary arm spacing

Acknowledgments

This work was carried out as part of the GRADECET (GRAvity DEpendence of Columnar to Equiaxed Transition in TiAl Alloys) research project and was funded by the European Space Agency (contract 4000114221/15/NL/PG). The view expressed herein can in no way be taken to reflect the official opinion of the European Space Agency. A part of the required high performance computing resources was provided by the EXPLOR center hosted by the University of Lorraine.

References

- [1] K. Kothari, R. Radhakrishnan, N. M. Wereley, Advances in gamma titanium aluminides and their manufacturing techniques, *Progress in Aerospace Sciences* 55 (2012) 1–16.
- [2] J. Aguilar, A. Schievenbusch, O. Kätzlitz, Investment casting technology for production of TiAl low pressure turbine blades—process engineering and parameter analysis, *Intermetallics* 19 (6) (2011) 757–761.
- [3] N. Reilly, B. Rouat, G. Martin, D. Daloz, J. Zollinger, Enhanced dendrite fragmentation through the peritectic reaction in TiAl-based alloys, *Intermetallics* 86 (2017) 126–133.
- [4] H. Rodot, L. Regel, A. Turtchaninov, Crystal growth of IV–VI semiconductors in a centrifuge, *Journal of crystal growth* 104 (2) (1990) 280–284.
- [5] G. Müller, G. Neumann, W. Weber, The growth of homogeneous semiconductor crystals in a centrifuge by the stabilizing influence of the Coriolis force, *Journal of crystal growth* 119 (1-2) (1992) 8–23.
- [6] N. Ramachandran, J. Downey, P. Curreri, J. Jones, Numerical modeling of crystal growth on a centrifuge for unstable natural convection configurations, *Journal of crystal growth* 126 (4) (1993) 655–674.
- [7] L. Yang, L. Chai, Y. Liang, Y. Zhang, C. Bao, S. Liu, J. Lin, Numerical simulation and experimental verification of gravity and centrifugal investment casting low pressure turbine blades for high Nb–TiAl alloy, *Intermetallics* 66 (2015) 149–155.

- [8] N. Reilly, Hétérogénéités de fabrication des aluminures de titane: caractérisation et maîtrise de leurs formations en coulée centrifuge, Ph.D. thesis, Université de Lorraine, Nancy, France, 2016.
- [9] V. Hatić, M. Cisternas-Fernández, B. Mavrič, M. Založnik, H. Combeau, B. Šarler, Simulation of a macrosegregation benchmark in a cylindrical coordinate system with a meshless method, *International Journal of Thermal Sciences* 142 (2019) 121 – 133, ISSN 1290-0729, doi:<https://doi.org/10.1016/j.ijthermalsci.2019.04.009>, URL <http://www.sciencedirect.com/science/article/pii/S1290072918319197>.
- [10] M. Cisternas Fernández, Modeling of solidification of TiAl alloys in centrifugal casting, Ph.D. thesis, Université de Lorraine, Nancy, France, 2019.
- [11] M. Cisternas Fernández, M. Založnik, H. Combeau, C. Huang, J. Zollinger, U. Hecht, Effect of the Coriolis force on the macrosegregation of aluminum in the centrifugal casting of Ti-Al alloys, in: *IOP Conference Series: Materials Science and Engineering*, vol. 529, IOP Publishing, 012033, 2019.
- [12] C. Beckermann, R. Viskanta, Double-diffusive convection during dendritic solidification of a binary mixture, *PhysicoChemical Hydrodynamics* 10 (2) (1988) 195–213.
- [13] S. Ganesan, D. Poirier, Conservation of mass and momentum for the flow of interdendritic liquid during solidification, *Metallurgical Transactions B* 21 (1) (1990) 173.
- [14] J. Ni, C. Beckermann, A volume-averaged two-phase model for transport phenomena during solidification, *Metallurgical Transactions B* 22 (3) (1991) 349.
- [15] D. Daloz, U. Hecht, J. Zollinger, H. Combeau, A. Hazotte, M. Založnik, Microsegregation, macrosegregation and related phase transformations in TiAl alloys, *Intermetallics* 19 (6) (2011) 749–756.
- [16] S. Battaglioli, A. Robinson, S. McFadden, Influence of natural and forced gravity conditions during directional columnar solidification, *International Journal of Heat and Mass Transfer* 126 (2018) 66–80.

- [17] P. Sung, D. Poirier, S. Felicelli, Simulating the initiation of a channel during directional solidification of a superalloy, *Metallurgical and Materials Transactions A* 32 (1) (2001) 202–207.
- [18] H. Combeau, M. Bellet, Y. Fautrelle, D. Gobin, E. Arquis, O. Budenkova, B. Dussoubs, Y. Du Terrail, A. Kumar, C.-A. Gandin, et al., Analysis of a numerical benchmark for columnar solidification of binary alloys, in: *IOP Conference Series: Materials Science and Engineering*, vol. 33, IOP Publishing, 012086, 2012.